

# Local anti-correlation between star-formation rate and gas-phase metallicity in disk galaxies

J. Sánchez Almeida<sup>1,2\*</sup>, N. Caon<sup>1,2</sup>, C. Muñoz-Tuñón<sup>1,2</sup>, M. Filho<sup>3,4</sup>, and M. Cerviño<sup>1,5</sup>

<sup>1</sup>*Instituto de Astrofísica de Canarias, E-38200 La Laguna, Tenerife, Spain*

<sup>2</sup>*Departamento de Astrofísica, Universidad de la Laguna, E-38205 La Laguna, Tenerife, Spain*

<sup>3</sup>*Center for Astrophysics and Gravitation - CENTRA/SIM, Departamento de Física, Instituto Superior Técnico, Universidade de Lisboa, Av. Rovisco Pais 1, P-1049-001 Lisbon, Portugal*

<sup>4</sup>*Departamento de Engenharia Física, Faculdade de Engenharia, Universidade do Porto, Rua Dr. Roberto Frias, s/n, P-4200-465, Oporto, Portugal*

<sup>5</sup>*Instituto de Astrofísica de Andalucía (IAA-CSIC), Apdo. 3004, 18008 Granada, Spain*

Accepted XXX. Received YYY; in original form ZZZ

## ABSTRACT

Using a representative sample of 14 star-forming dwarf galaxies in the local Universe, we show the existence of a spaxel-to-spaxel anti-correlation between the index  $N2 \equiv \log([\text{NII}]\lambda 6583/\text{H}\alpha)$  and the  $\text{H}\alpha$  flux. These two quantities are commonly employed as proxies for gas-phase metallicity and star formation rate (SFR), respectively. Thus, the observed  $N2$  to  $\text{H}\alpha$  relation may reflect the existence of an anti-correlation between the metallicity of the gas forming stars and the SFR it induces. Such an anti-correlation is to be expected if variable external metal-poor gas fuels the star-formation process. Alternatively, it can result from the contamination of the star-forming gas by stellar winds and SNe, provided that intense outflows drive most of the metals out of the star-forming regions. We also explore the possibility that the observed anti-correlation is due to variations in the physical conditions of the emitting gas, other than metallicity. Using alternative methods to compute metallicity, as well as previous observations of HII regions and photoionization models, we conclude that this possibility is unlikely. The radial gradient of metallicity characterizing disk galaxies does not produce the correlation either.

**Key words:** galaxies: star formation – galaxies: abundances – galaxies: evolution – galaxies: dwarf – galaxies: irregular

## 1 INTRODUCTION

Mannucci et al. (2010) and Lara-López et al. (2010) discovered that the scatter in the well-known mass-metallicity relation (MZR) correlates with the star-formation rate (SFR). Galaxies with a higher SFR show lower metallicity at a given stellar mass ( $M_\star$ ). This correlation between  $M_\star$ , SFR and gas-phase metallicity is called the fundamental metallicity relation (FMR), and its existence had been hinted at previously (Ellison et al. 2008; Peeples et al. 2009; López-Sánchez 2010). The FMR has gone through a close scrutiny during the last years, with some early works questioning its existence (e.g., Sánchez et al. 2013; Izotov et al. 2014; de los Reyes et al. 2015; Sanders et al. 2015; Kashino et al. 2016), but with a significantly larger number of confirmations (e.g., Salim et al. 2014; Andrews & Martini 2013; Yabe et al. 2012;

Wu et al. 2016; Ly et al. 2014, 2015; Amorín et al. 2014; Cullen et al. 2014; Maier et al. 2014; Brown et al. 2016), and with the correlation upholding to redshift 3 (Troncoso et al. 2014; Hidalgo 2017). The FMR is found to evolve with redshift so that metallicities at higher redshift are systematically lower given  $M_\star$  and SFR (e.g., Ly et al. 2014, 2015). There are also proposals to replace the SFR with the gas mass, which provides a deeper physical insight (Bothwell et al. 2013, 2016a,b), and reduces the dispersion of the relation (Jimmy et al. 2015). Lian et al. (2015) claim that stellar age, rather than SFR or gas mass, is the third parameter in the FMR (see also Sánchez Almeida et al. 2012).

The importance of the FMR is related to its physical cause. Current interpretations are always made in terms of the star formation feeding from metal-poor gas recently accreted by the galaxy disk. The advent of external gas does not change  $M_\star$ , but it decreases the mean metallicity of the gas, while simultaneously triggering star formation. Subse-

\* E-mail: jos@iac.es

quently, the star formation consumes the gas and produces metals that increase the gas metallicity through stellar winds and SNe, until new metal-poor gas arrives and the cycle repeats. This scenario was already suggested by [Mannucci et al. \(2010\)](#), and it has been refined using simple analytical models (e.g., [Brisbin & Harwit 2012](#); [Lilly et al. 2013](#); [Dayal et al. 2013](#); [Forbes et al. 2014](#); [Pipino et al. 2014](#)), as well as cosmological numerical simulations of galaxies with various degrees of sophistication ([Yates et al. 2012](#); [Romeo Velonà et al. 2013](#); [De Rossi et al. 2015](#); [Kacprzak et al. 2016](#)).

There are hints in literature that the anti-correlation between SFR and metallicity also occurs locally in galaxy disks, so that regions of high surface SFR are associated with drops in metallicity. The ten extremely metal-poor galaxies of the local Universe studied by [Sánchez Almeida et al. \(2015\)](#) have a large starburst with a metallicity between 5 and 10 times lower than the underlying host galaxy (see also [Sánchez Almeida et al. 2013, 2014b](#)). The same anti-correlation between SFR and metallicity was observed in three redshift 3 galaxies by [Cresci et al. \(2010\)](#). A large HII region at the edge of the dwarf galaxy GAMA J1411-00 provides most of the SFR of the galaxy, and has an oxygen abundance that is lower than the rest of the galaxy by  $\sim 0.2$  dex ([Richards et al. 2014](#)). The optical emission line analysis of the galaxy HCG 91c reveals that at least three HII regions harbour an oxygen abundance  $\sim 0.15$  dex lower than expected from their immediate surroundings and from the abundance gradient ([Vogt et al. 2015](#)). [Lagos et al. \(2016\)](#) find a slight anti-correlation between gas metallicity and SFR at spaxel scales, in the sense that higher SFRs are found in regions of lower metallicity (see their Fig. 11). Although the metallicity of IZw 18 is rather homogeneous, there is hint of scatter of approximately 0.2 dex, which anti-correlates with the SFR, as inferred from integrated H $\alpha$  flux ([Kehrig et al. 2016](#), Figs. 8 and 2).

This work presents evidence for the existence of such an anti-correlation between the local variations of SFR and gas-phase metallicity in more massive, more metallic star-forming galaxies. We use published 2D spectra (IFU<sup>1</sup> data) of blue compact galaxies, and the anti-correlation is present in 85% of the cases (Sect. 2). The observed anti-correlation is analyzed in terms of variable mixtures of metal-poor and metal-rich gas, and the closed-box evolution of the original metal-poor gas. Both possibilities account for the observed relation (Sect. 3). The metallicities are inferred using a strong-line ratio (explicitly,  $N2 \equiv \log([\text{NII}]\lambda 6583/\text{H}\alpha)$ ), whereas the SFR is derived from the H $\alpha$  flux. Variations in the properties of the local ionizing flux may induce spurious correlations between H $\alpha$  and N2, which could be incorrectly interpreted as variations in metallicity. Section 4.1 shows how the anti-correlation remains even when these variations are taken into account in the metallicity determination. Sections 4.2 and 4.3 are devoted to comparing the observed variations of line ratios with model predictions, to conclude that the observations seem to require variations in metallicity.

In Sect. 5 we refer to cosmological numerical simulations showing how this type of local anti-correlation can also result from the accretion of metal-poor gas that triggers the observed star formation bursts ([Ceverino et al. 2016](#); [Verbeke](#)

[et al. 2014](#)). This interpretation is not devoid of uncertainty, since it involves, in those galaxies showing the relation, either inefficient gas mixing in the galaxy disk, or the very recent accretion of metal-poor gas. The gas in the disk is expected to mix in a timescale of the order of the rotational period or smaller (e.g., [de Avillez & Mac Low 2002](#); [Yang & Krumholz 2012](#); [Petit et al. 2015](#)). Gas accretion, on the other hand, is theoretically predicted to fuel star formation in disk galaxies (e.g., [Dekel et al. 2009](#); [Silk & Mamon 2012](#)), but the observational evidence of this process is still rather indirect ([Sánchez Almeida et al. 2014a](#); [Sánchez Almeida 2017](#)).

## 2 THE OBSERVATIONAL RESULTS

### 2.1 The data

To carry out this study, we assembled a group of 18 blue star-forming galaxies, for which we have already produced maps of emission-line fluxes, line ratios, extinction, and gas kinematics. Among the group, 10 blue compact dwarf (BCD) galaxies were observed with PMAS-PPAK ([Roth et al. 2005](#)), with the data published in [Cairós et al. \(2009a\)](#), [Cairós et al. \(2009b\)](#) and [Cairós et al. \(2010\)](#), while the other 8 blue compact galaxies were observed with VIMOS ([Le Fèvre et al. 2003](#)), with the data published in [Cairós et al. \(2015\)](#).

The PMAS data cover an area of approximately  $16'' \times 16''$ , with a spatial sampling of  $1'' \times 1''$ , a spectral range from 3590 to 7000 Å, and a spectral resolution of approximately 7 Å. The VIMOS data cover an area of approximately  $27'' \times 27''$ , with a spatial sampling of  $0.67'' \times 0.67''$ . After combining blue grism and orange grism spectra, the spectral range goes from 4150 to 7400 Å, with a spectral resolution of approximately 2.0 Å. (More details about the PMAS and the VIMOS data can be found in [Cairós et al. 2010](#) and [Cairós et al. 2015](#), respectively.)

In this paper, we excluded two VIMOS galaxies from the analysis: Haro 15, which was only observed with the blue grism, and has neither H $\alpha$  nor  $[\text{NII}]\lambda 6583$  data, and Mrk 1131, which was only observed with the orange grism, and lacks the H $\beta$  data required to correct the H $\alpha$  fluxes for interstellar extinction. Thus, the final sample is made up of 16 galaxies, two of which will be discarded because they possess an AGN (Active Galactic Nucleus). Table 1 lists the main data characterizing the present sample of galaxies. Distances are employed in the paper to obtain absolute magnitudes and fluxes from the apparent magnitudes and fluxes, as well as to compute the scale in physical units (arcsec kpc<sup>-1</sup>). We use NED (NASA Extragalactic Database) values, which are corrected for local proper motions (more details in the caption of Table 1). Maps with their H $\alpha$  emission are given in Figs. 1 and 2, left column.

#### 2.1.1 Comments on three sources

Haro 11 and Mrk 409 represent two well-documented cases of AGNs among the sources in Table 1. They are discarded from our analysis because their emission lines are not excited by star formation, at least not exclusively (e.g., [Kewley et al.](#)

<sup>1</sup> Integral Field Unit

Table 1. Galaxy sample

Galaxy	RA	DEC	$m_B$	D	$M_B$	Sampling	Resolution	SFR	$\log M_\star$	Other designation
(1)	(2000)	(2000)	(mag)	(Mpc)	(mag)	(pc $''^{-1}$ )	(pc)	( $M_\odot \text{ yr}^{-1}$ )	( $\log M_\odot$ )	(11)
VIMOS										
Haro 11	00 36 52	-33 33 19	14.3 <sup>a</sup>	84.0	-20.3	410	550	19.9	9.5	ESO 350-IG 038
Haro 14	00 45 46	-15 35 49	13.7 <sup>b</sup>	13.0	-16.9	63	84	0.9	8.4	NGC 0244
Tol 0127-39	01 29 15	-39 30 38	16.2 <sup>c</sup>	71.3	-18.1	350	460	1.2	9.3	
Tol 1924-41	19 27 58	-41 34 32	14.0 <sup>b</sup>	42.4	-19.2	210	280	6.5	9.2	ESO 338-IG 004
Tol 1937-42	19 40 58	-42 15 45	15.1 <sup>b</sup>	41.1	-17.9	200	270	0.39	9.2	
Mrk 900	21 29 59	+02 24 51	14.2 <sup>b</sup>	18.9	-17.2	92	120	0.17	8.6	NGC 7077, UGC 11755
PMAS										
Mrk 1418	09 40 27	+48 20 16	13.9 <sup>b</sup>	14.6	-17.0	70	140	0.11	9.3	UGC 05151
Mrk 407	09 47 47	+39 05 04	15.4 <sup>a</sup>	27.2	-16.8	130	260	0.08	8.7	
Mrk 409	09 49 41	+32 13 16	14.4 <sup>b</sup>	26.3	-17.7	130	260	0.09	8.9	NGC 3011, UGC 5259
Mrk 32	10 27 02	+56 16 14	16.1 <sup>a</sup>	16.4	-14.9	80	160	0.02	7.8	
Mrk 750	11 50 02	+15 01 24	15.8 <sup>a</sup>	5.2	-13.3	25	50	0.02	7.0	
Mrk 206	12 24 17	+67 26 24	15.4 <sup>a</sup>	24.3	-16.9	120	240	0.32	9.2	
Tol 1434+03	14 37 08	+03 02 50	16.9 <sup>a</sup>	29.2	-15.5	140	280	0.06	7.7	SHOC 474
Mrk 475	14 39 05	+36 48 22	16.4 <sup>a</sup>	11.9	-14.2	58	120	0.05	8.6	
IZw 123	15 37 04	+55 15 48	15.4 <sup>a</sup>	15.4	-15.7	75	150	0.11	8.3	Mrk 487
IZw 159	16 35 21	+52 12 53	15.7 <sup>a</sup>	43.8	-17.2	210	420	0.39	9.0	Mrk 1499

Cols. (2) and (3): Units of right ascension are hours, minutes, and seconds, and units of declination are degrees, arcmin, and arcsec.  
 Col. (4):  $B$ -band apparent magnitudes: (a) magnitudes taken from HyperLeda (<http://leda.univ-lyon1.fr/>; [Paturel et al. 2003](#)); (b) integrated magnitudes from [Gil de Paz et al. \(2003\)](#), corrected for Galactic extinction; (c) asymptotic magnitudes obtained by extrapolating the growth curves, and corrected for Galactic extinction ([Cairós et al. 2001](#)); the asymptotic magnitudes listed in [Cairós et al. \(2001\)](#) were corrected for Galactic extinction following [Burstein & Heiles \(1982\)](#). Here they have been recomputed using the [Schlegel et al. \(1998\)](#) extinction curve.  
 Col. (5): Distance calculated using a Hubble constant of  $73 \text{ km s}^{-1} \text{ Mpc}^{-1}$ , and taking into account the effect of the Virgo Cluster, the Great Attractor, and the Shapley supercluster (from NED – <http://nedwww.ipac.caltech.edu/>).  
 Col. (6): Absolute magnitudes in the  $B$ -band, computed from the tabulated  $B$  apparent magnitudes and distances.  
 Col. (7): Plate scale.  
 Col. (8): Assuming two spaxels per resolution element.  
 Col. (9): SFR computed from the extinction-corrected  $H\beta$  fluxes for the integrated spectra published in [Cairós et al. \(2009a\)](#), [Cairós et al. \(2010\)](#), and [Cairós et al. \(2015\)](#), assuming  $F(H\alpha)/F(H\beta) = 2.86$  and using Eq. (2). For Mrk 409 ([Cairós et al. 2009b](#)), we used the sum of the fluxes of the 6 SF knots. As the  $H\alpha$  emission of the PMAS galaxies usually extends beyond the PMAS FOV, the corresponding SFRs are likely lower limits to the actual values.  
 Col.(10): Stellar mass inferred from the absolute magnitude and the colors using the mass-to-light ratios in [Bell & de Jong \(2001\)](#).

2013). However, they remain in some of the plots to evidence differences with the other galaxies.

Haro 11 displays three distinct components (Fig. 2, first row). The Eastern knot is associated with a young, high mass, X-ray binary ([Prestwich et al. 2015](#)) with ultraviolet emission ([Kunth et al. 2003](#)). The southern knot shows strong ultraviolet emission ([Kunth et al. 2003](#)). The central knot is coincident with HI observed in absorption ([MacHattie et al. 2014](#)), and harbors a luminous, compact, hard X-ray source, perhaps an intermediate mass black hole binary. The evidence for an accreting black hole is reinforced by the detection of a radio source ([Schmitt et al. 2006](#), and references therein). There is also strong evidence that Haro 11 is the result of a merger ([Östlin et al. 2015](#), and references therein). The BPT diagram of this galaxy (i.e.,  $O3 = \log([\text{OIII}]\lambda 5007/H\beta)$  versus  $N2 = \log([\text{NII}]\lambda 6583/H\alpha)$ ; after Baldwin, Phillips, and Terlevich 1981) clearly shows evidence for an AGN exciting the emission-line spectrum of this source.

Mrk 409 (Fig. 2, second row) shows a central star-forming component and an outer ring of star formation,

likely triggered by an expanding starburst-driven superbubble ([Cairós et al. 2009b](#)). Although there is no radio nor X-ray confirmation, the central source is associated with HeII  $\lambda 4686$  emission, and with a Seyfert 2-type AGN ([Moran et al. 2014](#)). The BPT diagram of this galaxy provides evidence of an AGN exciting the emission-line spectrum.

Only one galaxy in Table 1 presents signs of current interaction (Tol 1924-416). It is still included in the following analysis because its companion is quite distant (see below), and its emission lines behave as the other isolated galaxies. Tol 1924-416 appears to be composed of at least three star-formation knots (Fig. 1, third row). The source is documented as interacting with ESO 338-IG04B, 72 kpc away ([Cannon et al. 2004](#)). However, the distance is large compared with the physical size of the galaxy ( $\sim 5$  kpc effective radius), and so the companion is not expected to exert a significant tidal force on the galaxy (e.g., [Filho et al. 2015](#), Sect. 3.4).

## 2.2 The anti-correlation N2 versus H $\alpha$

Here we analyze the relationship between SFR, as measured from the H $\alpha$  flux, and metallicity, as parameterized by the N2 line ratio,

$$\text{N2} = \log([\text{NII}]\lambda 6583/\text{H}\alpha). \quad (1)$$

We first converted H $\alpha$  fluxes to SFRs by means of the formula (Kennicutt 1998),

$$\text{SFR}/(M_{\odot} \text{ yr}^{-1}) = 7.9 \times 10^{-42} L(\text{H}\alpha)/(\text{ergs s}^{-1}), \quad (2)$$

where the H $\alpha$  luminosity,  $L(\text{H}\alpha)$ , is corrected for extinction. The correction factor was computed, spaxel-by-spaxel, from the observed H $\alpha$ /H $\beta$  ratio, adopting the usual Case B low-density limit (Osterbrock & Ferland 2006), and the Cardelli et al. (1989) extinction law. As for the relationship between N2 and metallicity, we adopted the calibration,

$$12 + \log(\text{O}/\text{H}) = 9.07 + 0.79 \times \text{N2}, \quad (3)$$

proposed by Pérez-Montero & Contini (2009). The calibration we use for the SFR and the metallicity can be replaced by other similar calibrations in literature (e.g., Pettini & Pagel 2004; Kennicutt & Evans 2012; Morales-Luis et al. 2014) without modifying the main results in the paper.

Figure 1 show maps of H $\alpha$  flux (left column) and N2 (central column) for all the galaxies in our sample. Each row corresponds to one of the galaxies as labeled. A simple inspection shows that the peaks in H $\alpha$  flux tend to coincide with dips in N2, and vice-versa.

The anti-correlation is more apparent in the spaxel-by-spaxel scatter plot metallicity versus SFR. The third panel of each row in Fig. 1 contains the corresponding scatter plot. As the galaxies have different spatial samplings, we bring them to a common reference by plotting the surface SFR, in units of  $M_{\odot} \text{ yr}^{-1} \text{ kpc}^{-2}$ . As can be inferred from Fig. 1, right column, the anti-correlation between  $12 + \log(\text{O}/\text{H})$  and SFR goes from mild (e.g., Mrk 206) to very clear (e.g., Tololo 1924-416).

In order to quantify the correlation, we fit straight lines to the data points of the individual galaxies,

$$12 + \log(\text{O}/\text{H}) = m \times \log \text{SFR} + k, \quad (4)$$

where  $k$  and  $m$  are obtained using a variant of the least square fit method that takes into account uncertainties on both coordinates, as implemented in the FITEXY routine of the IDL<sup>2</sup> astro library. The values for the slope  $m$  and the intercept  $k$  are listed in Table 2. Figure 1, right column, shows the uncertainty of the individual values of  $12 + \log(\text{O}/\text{H})$  and SFR used by the fitting routine. To avoid overcrowding the figure, only errors at three representative SFRs are shown. They include measurement errors of the emission line fluxes, and the error of H $\alpha$ /H $\beta$  due to calibration uncertainties, which may be as large as 10% for the VIMOS data (see Cairós et al. 2015, for details). Excluding Haro 11 and Mrk 409, because they host an AGN (see Sect. 2.1.1), we find

$$\begin{aligned} m &= -0.15 \pm 0.07, \\ k &= 8.04 \pm 0.23, \end{aligned} \quad (5)$$

where the error bars represent the standard deviation among the fits for the different galaxies. We note a slight trend for the lower metallicity galaxies (smaller intercept) to show slightly more negative slopes. The error bars for the  $m$  and  $k$  of the individual galaxies are given in Table 2. They have been estimated using *bootstrapping*, which randomly resamples the original data and repeats the fit to evaluate the variance of the estimated parameters (e.g., Moore et al. 2003; Bradley & Tibshirani 1994).

Several sources of random noise affecting both SFR and  $12 + \log(\text{O}/\text{H})$  were not considered when estimating  $m$  and  $k$  in Eq. (5). However, the anti-correlation between SFR and metallicity remains in place even when they are included. Firstly, we analyze the fact that both SFR and  $12 + \log(\text{O}/\text{H})$  depend on the observed H $\alpha$  flux and so their errors are partly correlated. [NII] $\lambda 6583$  is a weak line, therefore, when its observed flux is dominated by noise, of roughly constant value in each map, then  $\text{N2} = \text{constant} - \log \text{H}\alpha$  (see Eq. [1]). In this case N2 drops when H $\alpha$  increases, giving rise to an artificial anti-correlation between SFR and  $12 + \log(\text{O}/\text{H})$  qualitatively similar to the observed one. The dotted lines in Fig. 1, right column, show the expected false correlation given the measured noise level in each [NII] $\lambda 6583$  map. As one can see, the artificial correlation is clearly unrelated to the observed correlation. To fully discard any influence of this bias, the points around the artificial correlation, indicated by red open symbols in the figures, have been excluded from all analyses. Secondly, the calibration in Eq. (3) assumes a one-to-one relation between N2 and  $12 + \log(\text{O}/\text{H})$ . However, this relation presents a significant intrinsic scatter due to differences in the properties of the HII regions (ionizing UV flux, ionizing parameter, and N to O ratio; see, e.g., Pérez-Montero & Díaz 2005). Pérez-Montero & Contini (2009) find a scatter of 0.34 dex given N2<sup>3</sup>. We carried out a Monte Carlo simulation to estimate whether such scatter could hinder the detection of the observed correlation between SFR and  $12 + \log(\text{O}/\text{H})$ . Mock observations were produced starting from a uniform random distribution of SFRs in the range of the observed values (from 0.01 to  $10 M_{\odot} \text{ kpc}^{-2} \text{ yr}^{-1}$ ), and then computing the associated metallicity as  $12 + \log(\text{O}/\text{H}) = m \times \text{SFR} + k$ , with  $m$  and  $k$  given by Eq. (5). Random gaussian noise with a standard deviation of 0.34 dex was added to  $12 + \log(\text{O}/\text{H})$ . One thousand mock observations were produced assuming 200 spaxels per galaxy, which is a realistic number for the spaxels in the VIMOS fields. These mock observations were analyzed as real observations, fitting straight lines to retrieve 1000 different values for  $m$  and  $k$ . The mean slope turns out to be  $-0.15 \pm 0.03$ , with the error bar representing the dispersion among the 1000 individual estimates of  $m$ . If 100 spaxels per galaxy are considered, the dispersion increases only

<sup>3</sup> Part of this scatter is not applicable to the within-galaxy variation studied in this paper. Pérez-Montero & Contini consider galaxies with large differences in N/O which are not present in a single galaxy (see Sect. 4.1). They also use line ratios from very heterogeneous bibliographic sources, so that part of the scatter is not intrinsic to the calibration but attributable to observational errors in the employed data. Thus, other similar calibrations based on N2 present much smaller scatter, like the 0.18 dex quoted by Pettini & Pagel (2004). Therefore, this 0.34 dex scatter should be regarded as an upper limit to the intrinsic error of the N2 calibration.

<sup>2</sup> Interactive Data Language

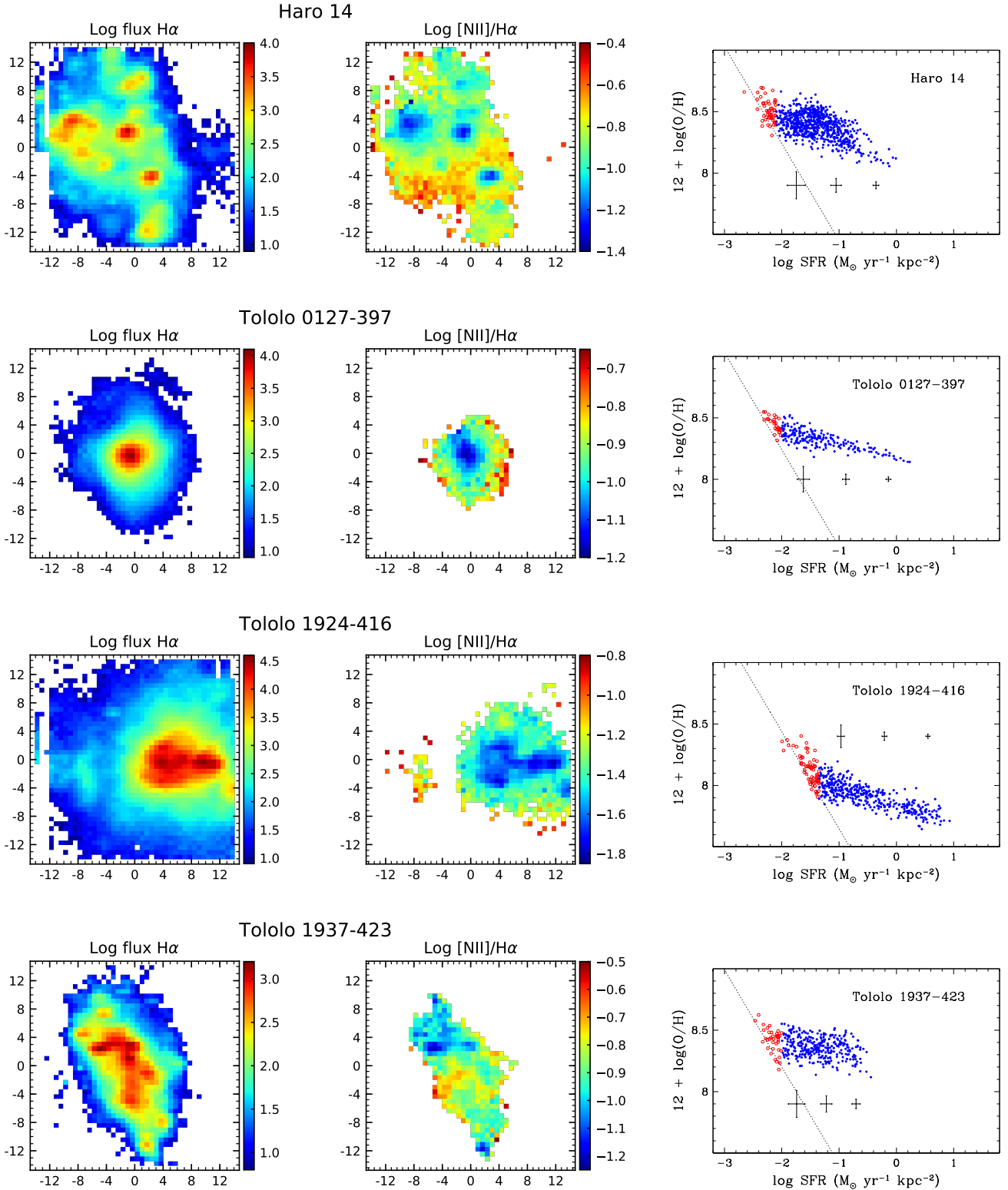


**Figure 1.** Left and central columns: maps of H $\alpha$  (left) and [NII] $\lambda$ 6583/H $\alpha$  (center), both in logarithmic scale, for the galaxies studied in the paper. Each row corresponds to one galaxy as labelled. The VIMOS data cover an area of approximately  $27'' \times 27''$  with a spatial sampling of  $0.67'' \times 0.67''$ . The area covered by PMAS is  $16'' \times 16''$  with a sampling of  $1'' \times 1''$ . Note the anti-correlation between the peaks and dips in the two maps. The fluxes in H $\alpha$  are given in units of  $10^{-16}$  erg s $^{-1}$  cm $^{-2}$ . Right column: scatter plots metallicity versus surface SFR. Noise in the spectra may induce an artificial correlation, represented as dotted lines in the individual panels (see main text). Such artifact does not explain the observed correlation except perhaps for the red points, which have been excluded from the analysis. The typical error bars for  $12 + \log(\text{O}/\text{H})$  and SFR at three representative SFRs are also shown in each panel. These error bars do not include the error introduced by the calibration to infer  $12 + \log(\text{O}/\text{H})$  from N2, which is probably significantly larger than the bars on display. The consequences of the calibration error on the relation are discussed in the main text. MNRAS **000**, 1–18 (2018)

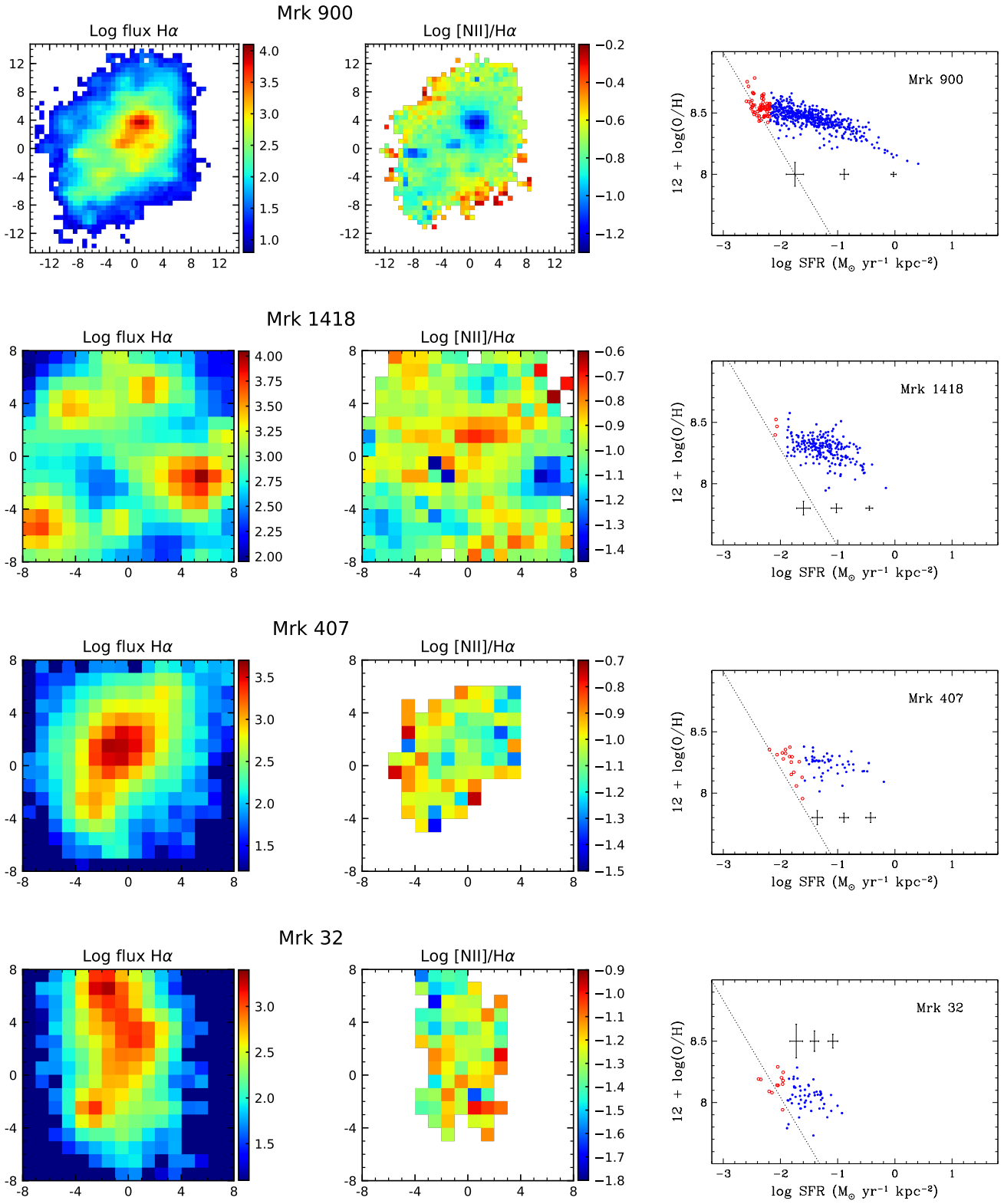


Figure 1. Continued.

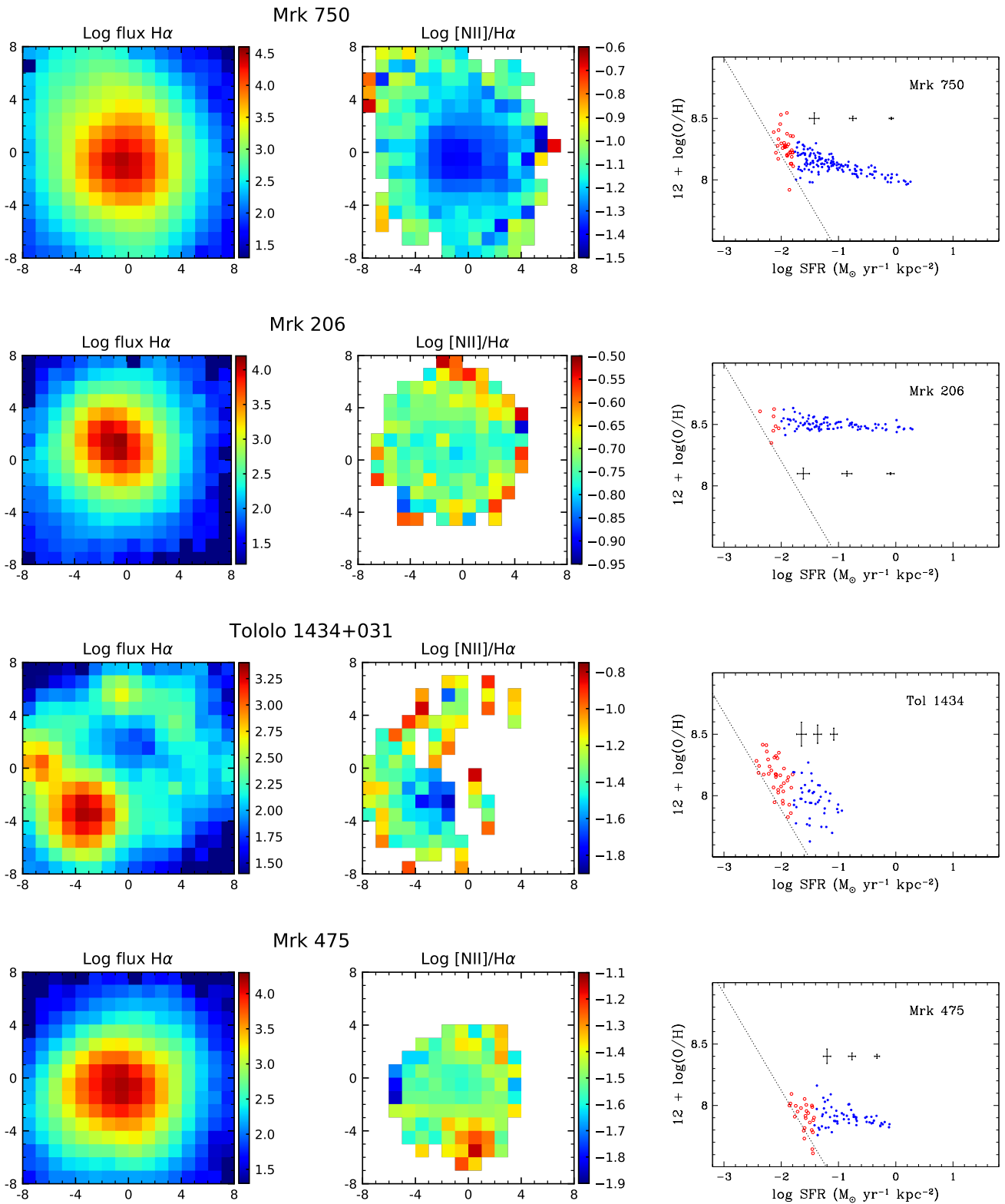


Figure 1. Continued.

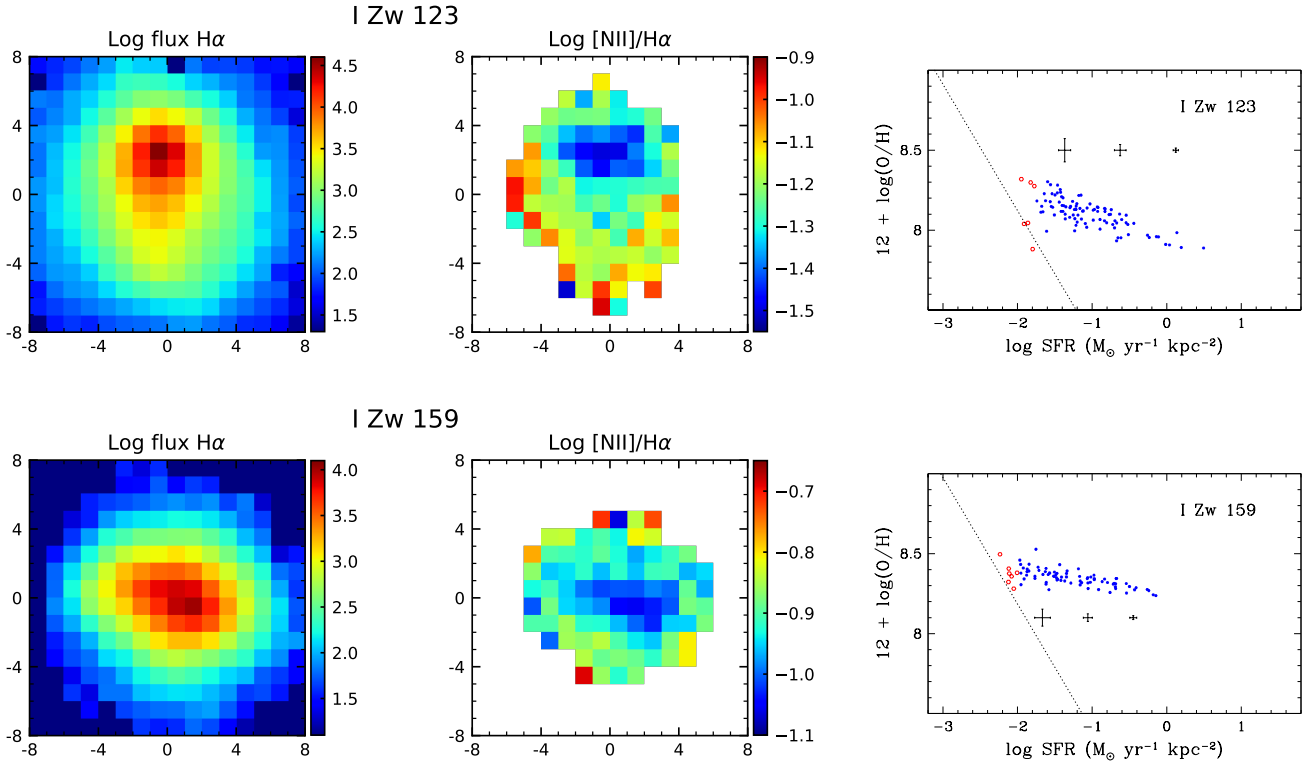


Figure 1. Continued.

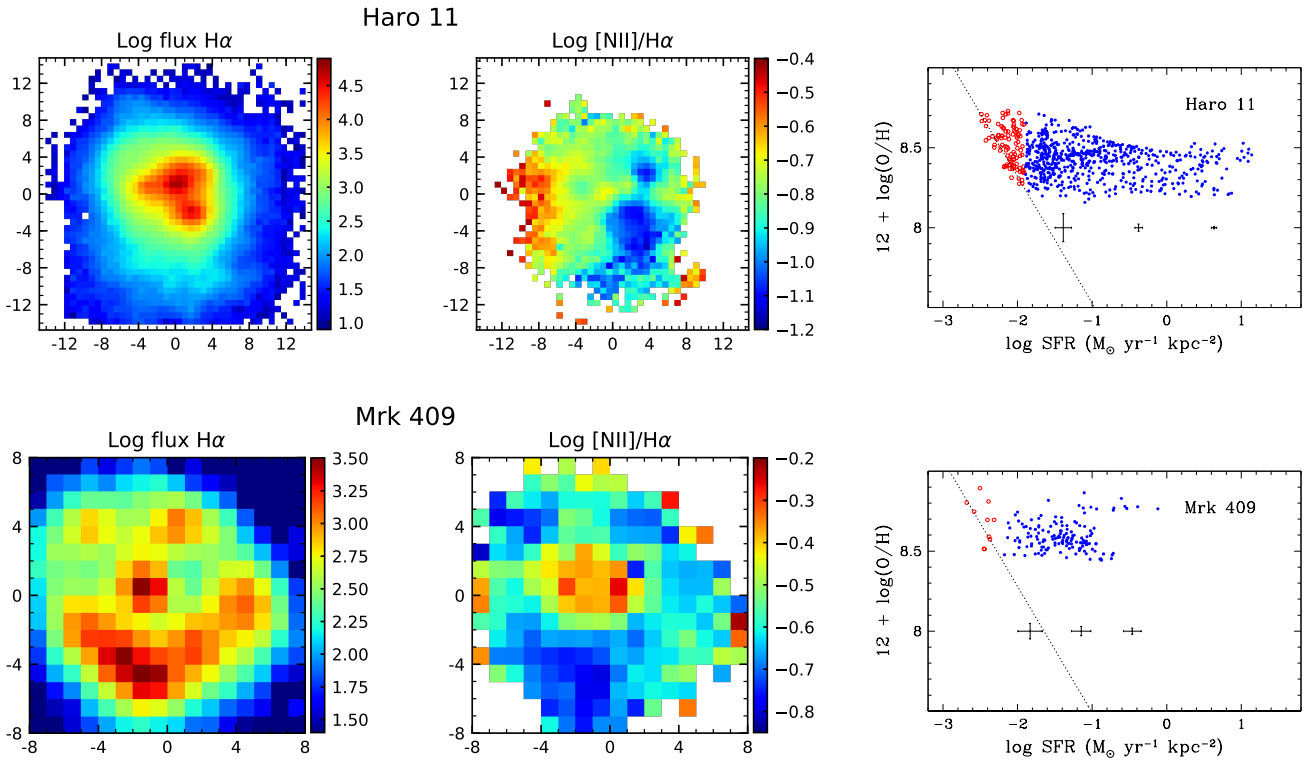


Figure 2. Same as Fig. 1 with the two well-documented cases of AGNs. They are not included in our analysis. Note that the scatter plots metallicity versus surface SFR (third column) show no obvious trend, in contrast with many of the star-forming galaxies in Fig. 1.



**Table 2.** Parameters that characterize the anti-correlation  $12+\log(\text{O/H})$  versus SFR.

Galaxy	$m^a$	$k^a$	$m^b$	$k^b$	$Z_1/Z_\odot^c$	$1/N_{eff}^c$	$Z_1/Z_\odot^d$	$Y_{eff}/N/Z_\odot^e$
Haro 11	$+0.023 \pm 0.042$	$8.402 \pm 0.011$	$-0.031 \pm 0.005$	$8.390 \pm 0.061$		No correlation		
Haro 14	$-0.232 \pm 0.009$	$8.079 \pm 0.010$	$-0.147 \pm 0.009$	$8.181 \pm 0.012$	0.000	$0.205 \pm 0.009$	$0.283 \pm 0.011^*$	$0.087 \pm 0.004$
Tol 0127	$-0.117 \pm 0.005$	$8.176 \pm 0.008$	$-0.108 \pm 0.005$	$8.180 \pm 0.005$	0.000	$0.113 \pm 0.005$	$0.303 \pm 0.006^*$	$0.042 \pm 0.002$
Tol 1924	$-0.143 \pm 0.008$	$7.854 \pm 0.004$	$-0.138 \pm 0.007$	$7.846 \pm 0.005$	$0.054 \pm 0.031$	$0.251 \pm 0.070$	$0.115 \pm 0.002$	$0.020 \pm 0.001$
Tol 1937	$-0.101 \pm 0.018$	$8.234 \pm 0.023$	$-0.063 \pm 0.012$	$8.274 \pm 0.018$	0.000	$0.094 \pm 0.065$	$0.381 \pm 0.013$	$0.045 \pm 0.009$
Mrk 900	$-0.190 \pm 0.008$	$8.195 \pm 0.011$	$-0.136 \pm 0.007$	$8.252 \pm 0.010$	0.000	$0.183 \pm 0.008$	$0.332 \pm 0.019^*$	$0.083 \pm 0.003$
Mrk 1418	$-0.238 \pm 0.019$	$8.008 \pm 0.023$	$-0.138 \pm 0.017$	$8.114 \pm 0.023$	0.000	$0.197 \pm 0.031$	$0.248 \pm 0.021$	$0.073 \pm 0.007$
Mrk 407	$-0.079 \pm 0.026$	$8.150 \pm 0.028$	$-0.069 \pm 0.036$	$8.153 \pm 0.038$	0.000	$0.057 \pm 1.466$	$0.311 \pm 0.015$	$0.021 \pm 0.009$
Mrk 409	$-0.344 \pm 0.284$	$8.148 \pm 0.336$	$+0.026 \pm 0.025$	$8.630 \pm 0.038$		No correlation		
Mrk 32	$-0.185 \pm 0.060$	$7.804 \pm 0.089$	$-0.097 \pm 0.061$	$7.891 \pm 0.088$	0.000	$0.116 \pm 0.075$	$0.182 \pm 0.020$	$0.027 \pm 0.013$
Mrk 750	$-0.121 \pm 0.005$	$8.001 \pm 0.005$	$-0.106 \pm 0.009$	$8.008 \pm 0.007$	$0.024 \pm 0.199$	$0.124 \pm 0.049$	$0.197 \pm 0.003$	$0.027 \pm 0.002$
Mrk 206	$-0.025 \pm 0.008$	$8.473 \pm 0.007$	$-0.028 \pm 0.006$	$8.470 \pm 0.008$	$0.592 \pm 0.430$	$0.465 \pm 0.328$	$0.600 \pm 0.011$	$0.014 \pm 0.005$
Tol 1434	$-0.294 \pm 0.059$	$7.579 \pm 0.081$	$-0.205 \pm 0.081$	$7.670 \pm 0.114$	$0.140 \pm 0.044$	$0.794 \pm 0.728$	$0.128 \pm 0.017$	$0.036 \pm 0.016$
Mrk 475	$-0.119 \pm 0.016$	$7.821 \pm 0.008$	$-0.061 \pm 0.026$	$7.851 \pm 0.016$	0.000	$0.088 \pm 0.068$	$0.139 \pm 0.004$	$0.015 \pm 0.002$
I Zw 123	$-0.161 \pm 0.012$	$7.944 \pm 0.010$	$-0.148 \pm 0.012$	$7.947 \pm 0.011$	$0.087 \pm 0.192$	$0.262 \pm 0.070$	$0.160 \pm 0.006^*$	$0.032 \pm 0.004$
I Zw 159	$-0.088 \pm 0.007$	$8.240 \pm 0.007$	$-0.076 \pm 0.009$	$8.251 \pm 0.009$	0.000	$0.084 \pm 0.033$	$0.370 \pm 0.007^*$	$0.036 \pm 0.003$

<sup>a</sup> Slope and intercept defined in Eq. (4), computed considering measurement errors in the emission line fluxes.

<sup>b</sup> Slope and intercept defined in Eq. (4), computed adding 0.34 dex to the measurement errors in  $12+\log(\text{O/H})$ .

<sup>c</sup> Metallicity of the metal-poor gas and inverse index of the Kennicutt-Schmidt relation; Eqs. (8) and (10).

<sup>d</sup> Based on Eq. (8) with  $N = 1.4$ . The superscript (\*) points out when the fit worsens with respect to the case where  $1/N_{eff}$  is inferred from the fit.

<sup>e</sup> Effective yield from Eqs. (12) and (13).

moderately, with  $m = -0.150 \pm 0.04$ . The dispersion inferred from the Monte Carlo simulation is significantly smaller than the observed value, therefore, a random noise of 0.34 dex in metallicity does not impede finding and characterizing the slope of a correlation between SFR and  $12 + \log(\text{O/H})$  like the one we obtain (Eq. [5]). We completed this Monte Carlo simulation with a direct estimate of the effect on the fit of having a 0.34 dex extra error in  $12 + \log(\text{O/H})$ . For every single galaxy, the linear fit was repeated adding in quadrature 0.34 dex to the error in  $12 + \log(\text{O/H})$ . The inferred values are consistent with the values given in Eq. (5), explicitly,  $m = -0.11 \pm 0.05$  and  $k = 8.08 \pm 0.21$ , with the error bars representing the scatter among the galaxies in our sample. Table 2 includes the slope and intercept ( $m$  and  $k$ ) once the 0.34 dex extra error is included in the least squares fitting procedure. The list also includes formal error bars which have been evaluated using bootstrapping, as we did with the original estimate.

### 2.3 Spatial resolution compared with the physical size of the HII regions

The spatial resolution of the maps is listed in Table 1. We estimate the resolution as twice the sampling interval, following the Shannon sampling theorem. The observed values span from 50 to 500 pc, with the typical value around 200 pc. These sizes are significantly larger than the expected size of an HII region, and comparable to the size of giant HII regions. For example, the Strömgren radius of the model HII regions are all smaller than 200 pc, provided that the mass of the ionizing stellar cluster is smaller than  $10^6 M_\odot$  (e.g., Villaverde et al. 2010). Similarly, the observed HII regions have diameters consistent with this range in sizes (e.g., Fuentes-Masip et al. 2000; Hunt & Hirashita 2009; Wisnioski et al. 2012; Hinojosa-Goñi et al. 2016; Olmo-García et al. 2017). The

fact that the spatial resolution is coarser than the typical HII region size implies that, to first order, the individual resolution elements in our maps spatially integrate the signal coming from full HII regions. This fact justifies the analysis made Sect. 4, where the properties observed in each spaxel are compared with the properties of integrated HII regions.

### 2.4 Correlation after subtracting the running mean average

The correlation described in the Sect. 2.2 is dominated by *local variations* in N2 and H $\alpha$ . It is not due to large-scale variations, like the radial gradients of metallicity typical of massive spirals, including the Milky Way (e.g., Pagel & Edmunds 1981; Sánchez et al. 2014). In order to show this result, we have repeated the plot  $12+\log(\text{O/H})$  versus SFR in Fig. 1, this time removing a running-mean local value from the original signal. This high-pass spatial filtering leaves only the small scale variations in the images of N2 and H $\alpha$ . The result for the VIMOS galaxies is shown in Fig. 3. The anti-correlation between N2 and H $\alpha$  remains with an amplitude similar to the amplitude in the original images (cf. Figs. 1 and 3). The subtracted running mean images were produced using a box of  $5 \times 5$  spaxels. The fact that the correlation remains after removing a running-mean average also holds for the galaxies in the PMAS sample.

## 3 ANALYSIS IN TERMS OF A CORRELATION BETWEEN METALLICITY AND SFR

Here we explore possible explanations for the observed relation between N2 and H $\alpha$  in terms of a local correlation between metallicity and SFR. We analyze the mixing of pre-existing gas with variable amounts of metal-poor gas, as ex-

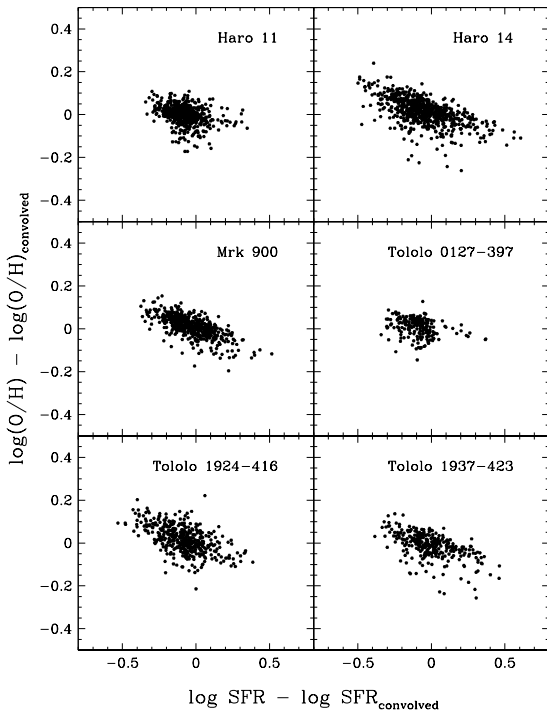


**Figure 3.** Similar to the panels on the right column of Fig. 1, except that running-mean average images have been subtracted from the original  $12+\log(\text{O}/\text{H})$  and SFR images. The anti-correlation between the excess of metallicity,  $12+\log(\text{O}/\text{H})-12+\log(\text{O}/\text{H})_{\text{convolved}}$  and the excess of SFR,  $\log \text{SFR}-\log \text{SFR}_{\text{convolved}}$ , remains with an amplitude similar to that of the correlation of the original images (cf. Fig. 1). The units of the axes are the same as in Fig. 1.

pected from external metal-poor gas accretion (Sect. 3.1), and the self-enrichment due to local variations of the star-formation history (Sect. 3.2). Variations of the physical conditions in the emitting nebula other than metallicity are treated in Sect. 4. This last option would forge a relation between  $12+\log(\text{O}/\text{H})$  and SFR. As we describe in Sect. 4, this possibility is unlikely, although it cannot be completely ruled out.

### 3.1 Mixing of metal-rich with metal-poor gas

One possibility to explain the observed correlation is assuming that the mass of gas producing stars,  $M_g$ , is a mixture of pre-existing metal-rich gas of mass  $M_{g2}$ , blended together with variable masses of metal-poor gas,  $M_{g1}$ , i.e.,

$$M_g = M_{g1} + M_{g2},$$

$$M_g Z = M_{g1} Z_1 + M_{g2} Z_2, \quad (6)$$

with  $Z_1$ ,  $Z_2$ , and  $Z$  the metallicity of the metal-poor gas, the metallicity of the metal-rich gas, and the metallicity of the mixture, respectively. This scenario is to be expected if the

star formation in each galaxy is triggered by the accretion of pristine or nearly-pristine gas falling onto the disk. Depending on the mass of gas that ends up in each particular location on the disk, starbursts with different combinations of metallicity and SFR are produced. The metallicity is given by Eq. (6), whereas the (surface density) SFR is given by the (surface density) gas mass through the so-called Kennicutt-Schmidt relation (e.g., Kennicutt 1998),

$$\text{SFR} \propto M_g^N, \quad (7)$$

with  $N \simeq 1.4$  (Kennicutt & Evans 2012). Using Eqs. (6) and (7), one obtains

$$Z = Z_1 + (Z_2 - Z_1) \times (\text{SFR}_2/\text{SFR})^{1/N}, \quad (8)$$

where  $\text{SFR}_2$  represents the SFR to be observed if there is no external gas infall ( $M_{g1} = 0$ ).

Equation (8) predicts an anti-correlation between the metallicity  $Z$  and the SFR that accounts for the observed trend (Sect. 2) once the free parameters in the relation are tuned. If all the spaxels start off with the same gas mass,  $M_{g2}$ , then Eq. (8) predicts that  $Z$  will vary as  $\text{SFR}^{1/N}$ , with  $1/N \sim 0.71$  (Kennicutt & Evans 2012). On the other hand, if different spaxels begin with different  $M_{g2}$ , then  $M_g$  and  $M_{g2}$  are correlated, so that

$$M_{g2}/M_g \simeq (\langle M_{g2} \rangle / M_g)^\delta, \quad (9)$$

with  $\delta \ll 1$  (Appendix A). The parameter  $\langle M_{g2} \rangle$  stands for an appropriate constant scaling factor. In this case, Eq. (8) still holds, replacing  $\text{SFR}_2$  with  $\langle \text{SFR}_2 \rangle$ , and replacing  $1/N$  with the exponent  $1/N_{\text{eff}}$  given by

$$1/N_{\text{eff}} = \delta/N \ll 1/N. \quad (10)$$

Examples of the fits to Eq. (8) are shown in Figures 4 and 5. They were performed using the MPFIT<sup>4</sup> package implemented in IDL. The fits were constrained to have  $Z_1 \geq 0$ . Table 2 contains the free parameters inferred from the fits for these and the remaining galaxies. If  $1/N$  is assumed to be a free parameter, the fits are excellent (see the red solid lines in Figs 4 and 5). However, one obtains a value for  $1/N$  very different from the expected value  $1/N \simeq 0.71$  ( $N = 1.4$ ). If, on the other hand,  $1/N$  is set to 0.71, the fit often worsens (compare the red and the green lines in Fig. 4; the 5 galaxies where this fit worsens are marked with an asterisk in Table 2). Table 2 summarizes the values for  $1/N_{\text{eff}}$  obtained in the various fits. Its mean and standard deviation are given by

$$1/N_{\text{eff}} = 0.20 \pm 0.19, \quad (11)$$

which, assuming  $N = 1.4$ , renders a value of  $\delta = 0.28 \pm 0.26$ . This low value is consistent with the Monte Carlo simulation given in Appendix A, which was carried out assuming that the two masses,  $M_{g1}$  and  $M_{g2}$ , are similar ( $M_{g1}$  only 50% larger than  $M_{g2}$ ), with their spaxel-to-spaxel variation being also similar.

As one can see in Table 2, the metallicity of the external gas,  $Z_1$ , tends to be zero, i.e., at the limit forced by the constrained fit. We interpret this fact as an indication that the observed correlation is consistent with the infall of

<sup>4</sup> A non-linear least-squares minimization procedure described by Markwardt (2009).

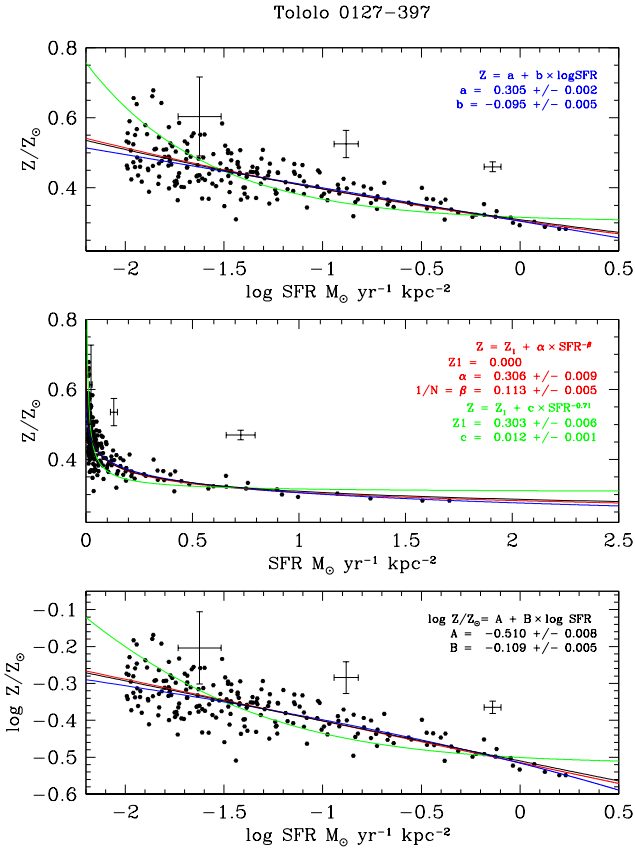


**Figure 4.** Metallicity ( $Z$ ) versus SFR for Tololo 0127-397 (black solid circles). The three panels show the same points and curves in three different representations;  $Z$  versus log SFR (top),  $Z$  versus SFR (middle) and log  $Z$  versus log SFR (bottom). The red line is the best fit to Eq. (8), obtained by leaving the exponent, and the slope free (see the inset in the middle panel), but forcing  $Z_i \geq 0$ . The green line also represents a fit to Eq. (8), but setting  $N = 1.4$  (corresponding to  $1/N = 0.71$ ). The cyan line is the best linear fit to Eq. (12) (see inset in the top panel). Finally, the black line represents a linear fit in the log-log plane as parameterized in Eq. (4). To convert  $12 + \log(\text{O}/\text{H})$  to metallicity in solar units, we adopted  $12 + \log(\text{O}/\text{H})_{\odot} = 8.69$ , from [Asplund et al. \(2009\)](#). The value of the best-fitting parameters, together with the formal uncertainties from the fitting algorithm, are also shown. The green line provides a fit that it clearly worse than the fit represented by the other three lines. This happens only with some of the galaxies; often, the four mathematical models are indistinguishable (see Fig. 5). As in Fig. 1, typical error bars (vertically shifted for clarity) are shown at three representative SFR values.

very metal-poor gas, although the actual metallicity remains unconstrained.

### 3.2 Self-contamination in open-box evolution

Another possibility that qualitatively explains the observed anti-correlation between metallicity and SFR is self-contamination due to star formation. If the whole galaxy disk starts off with similar amounts of metal-poor gas per unit surface, those regions where the stellar evolution proceeds faster will consume the gas earlier, and will become

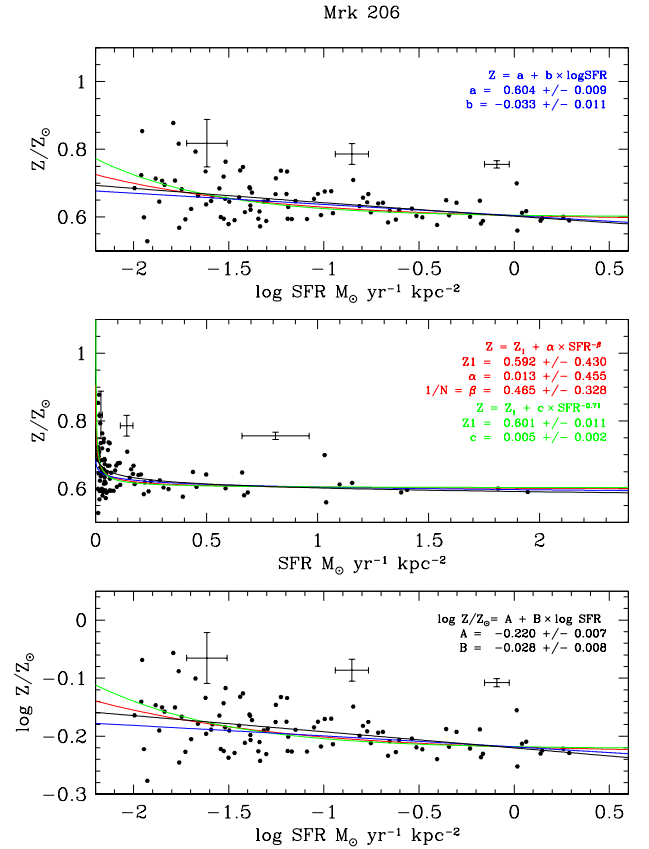


**Figure 5.** Same as Fig. 4 for Mrk 206. In this case, all four mathematical models fit the data points satisfactorily.

richer in metals. The differences between different regions can be due to the stochastic nature of the star-formation process. Under these hypotheses, a simple close-box evolution model (e.g., [Tinsley 1980](#)) and the Kennicutt-Schmidt relation (Eq. [7]) render,

$$Z = Z_i - Y \frac{\ln 10}{N} \log(\text{SFR}/\text{SFR}_i), \quad (12)$$

where  $Y$  designates the oxygen yield (e.g., [Meynet & Maeder 2002](#)), and  $Z_i$  and  $\text{SFR}_i$  represent the initial metallicity and SFR, respectively. The above equation can be generalized to an open-box evolution, where part of the metal-enriched gas escapes from the region by star-formation-driven outflows. In this case, one must replace the yield  $Y$  with the *effective* yield  $Y_{eff}$  (e.g., [Sánchez Almeida et al. 2015](#)),

$$Y_{eff} = Y \frac{1 - R}{1 - R + W}, \quad (13)$$

where  $R$  represents the so-called return fraction (i.e., the fraction of gas returned to the interstellar medium by supernova explosions and stellar winds per unit mass locked into stars), and  $W$  is the mass loading factor, i.e., the outflow rate in units of the SFR. In practice,  $Y_{eff} \ll Y$  since  $R \ll 1$  and  $W$  is often large (see the paragraph below). The oxygen yield is believed to be  $Y \approx 0.004$  for metallicities smaller than the solar metallicity ([Meynet & Maeder 2002](#)). Then,

using the value for the solar metallicity from [Asplund et al. \(2009\)](#),  $Y/Z_{\odot} \simeq 0.70$ .

Examples of fits to the observed relation  $Z$  versus SFR using Eq. (12) are shown as the solid blue lines in Figs. 4 and 5. Given the scatter of the data, the fits are as good as the fits to Eq. (8) (the red solid lines) and the generic straight line in Eq. (4) (the black solid lines). This statement holds for all the galaxies, with the free parameters of the fit given in Table 2. The main observational constraint set by the parameters resulting from fitting Eq. (12) is the need for intense outflows, capable of carrying away most of the metals produced in each starburst. Specifically, the mean and standard deviation of  $Y_{eff}/N$  is

$$Y_{eff}/N = (0.040 \pm 0.025) Z_{\odot}, \quad (14)$$

so that using typical values for  $R = 0.3$  (e.g., [Sánchez Almeida et al. 2014a](#)),  $Y/Z_{\odot} \simeq 0.70$ , and  $N = 1.4$ , Eq. (13) renders,

$$W = 11.3 \pm 6.7. \quad (15)$$

This value for  $W$  is large, but it is consistent with some of the large values found in local dwarf galaxies (see [Veilleux et al. 2005](#); [Olmo-García et al. 2017](#), and references therein). Moreover,  $W$  refers to the mass expelled from each spaxel, which does not imply that the gas returns back all the way to the inter-galactic medium. If it only reaches the circumgalactic medium, it may fall back onto the galaxy disk as part of a galactic fountain (e.g., [Fraternali 2017](#); [Rubin 2017](#); [Muratov et al. 2017](#)). Stellar feedback processes of the required magnitude should be accompanied by shells and bubbles of swept material visible in emission lines (e.g., [Simpson et al. 2012](#); [Olmo-García et al. 2017](#)).

#### 4 ARE METALLICITY VARIATIONS NEEDED TO EXPLAIN THE ANTI-CORRELATION?

The metallicities are inferred from the N2 index, whereas the SFR is derived from the  $H\alpha$  flux (Sect. 2). The two quantities are proxies for the true metallicity and the true SFR, respectively, and they are subject to systematic errors. Thus, spatial variations in the properties of the local ionizing flux may induce a correlation between N2 and  $H\alpha$  (e.g., [Morales-Luis et al. 2014](#)), which could be (mis)interpreted as a correlation between metallicity and SFR. This section is devoted to arguing that the observed spatial variation of line fluxes do require a change in metallicity, so that interpretations such as those provided in Sects. 3.1 and 3.2 are needed. In other words, they cannot be produced only by systematic errors resulting from the variation in mass and age of the stellar cluster that ionize each spaxel, and the change in ionization parameter that results.

As we explain in Sect. 2.3, the spatial resolution of the IFU maps used in our work is too coarse to resolve individual HII regions. Therefore, each typical spaxel integrates the spectrum of one or several full HII regions. This hypothesis is underlying the following discussion.

##### 4.1 Alternative estimate of the metallicities

The use of the N2 index as a proxy for metallicity does not consider differences in physical parameters between HII regions with the same metallicity. In order to check whether

the existing differences can mimic an anti-correlation between SFR and O/H, we have used another alternative method that considers differences in N/O and ionization parameters to infer the oxygen abundance. The code HII-CHEMISTRY (HIIC) by [Pérez-Montero \(2014\)](#) compares line ratios of a number of selected emission lines with the predictions of a grid of CLOUDY ([Ferland et al. 2013](#)) photoionization models having different physical conditions, including different N/O and ionization. Changes in N/O account for peculiarities in the chemical composition of the HII region, whereas the ionization parameter is related to the age and mass of the ionizing stellar cluster as well as to the geometry of the gas. HIIC has been thoroughly tested, providing results identical to the direct method within around 0.1 dex in a large variety of objects ([Pérez-Montero 2014](#)), including those with SFR and metallicity similar to our galaxies (e.g., [Sánchez Almeida et al. 2016](#), Fig. 3).

HIIC can use different emission lines depending on availability. In the case of the galaxies observed with PMAS, the list of lines includes [OII] $\lambda$ 3727, [OIII] $\lambda$ 5007, [NII] $\lambda$ 6583, [SII] $\lambda$ 6716,6731, as well as  $H\alpha$  and  $H\beta$ . The VIMOS spectra do not include [OII], and this particular line cannot not be used in the metallicity estimate. Figure 6 shows the scatter plot  $12+\log(O/H)$  versus SFR for the four VIMOS galaxies chosen to compute O/H with HIIC. The four examples were selected because they show a clear anti-correlation when O/H is computed using N2 (Fig. 1). The same anti-correlation is maintained even when this other more accurate technique for measuring O/H is used. Figure 6 includes the linear fit to the anti-correlation obtained when  $12+\log(O/H)$  is based on N2 ( $k$  and  $m$  in Table 2). The slopes of the anti-correlation inferred from N2 agree remarkably well with the distribution of points obtained using HIIC (Fig. 6).

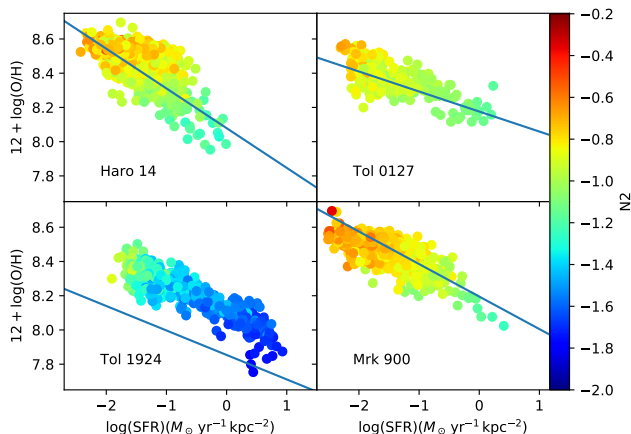
Similar agreement between N2-based and HIIC-based metallicity is found when comparing PMAS galaxies (Fig. 7), which have less spatial resolution but include [OII]. In the case of the PMAS galaxies, HIIC has a direct observational constraint on the ionization through the ratio [OII]/[OIII]. As for the VIMOS galaxies, these examples were chosen to apply HIIC because they show a clear anti-correlation when O/H is computed using N2. The symbols in Figs. 6 and 7 have been color-coded according to N2, which clearly shows an increase with increasing metallicity, thus explaining why the two methods of estimating O/H depict the same anti-correlation between metallicity and SFR.

Figure 8 illustrates how the ionization parameter ( $U$ ) and N/O vary with SFR according to HIIC. The galaxies show a significant increase of  $U$  with increasing SFR, whereas N/O remains rather constant across the galaxy. Figure 8 includes VIMOS galaxies, but the behavior is very similar for PMAS objects.

To summarize, even when the within-galaxy spread in N/O and ionization parameter is considered, the anti-correlation between metallicity and SFR remains.

##### 4.2 Comparison with observed HII regions

The argumentation will be based on the position of the individual spaxels of the analyzed galaxies in the BPT diagram (O3 versus N2; [Baldwin et al. 1981](#)). The position of the data points in this plane is very sensitive to both the ionizing spectrum and the metallicity of the emitting gas (e.g.,



**Figure 6.**  $12 + \log(\text{O}/\text{H})$  versus SFR for four VIMOS galaxies (see the labels), with the oxygen abundance provided by HIIC (Pérez-Montero 2014). HIIC considers changes in N/O and ionization parameter within the galaxies. The anti-correlation between O/H and SFR that appears in Fig. 1 remains here. The solid lines show the linear fits to the anti-correlation in Fig. 1 ( $k$  and  $m$  in Table 2). The different spaxels are color-coded according to N2, as indicated by the color bar. The formal error bars for  $12 + \log(\text{O}/\text{H})$  turn out to be around 0.04 dex, which are inferred by HIIC from the difference between the model and the observed line fluxes.

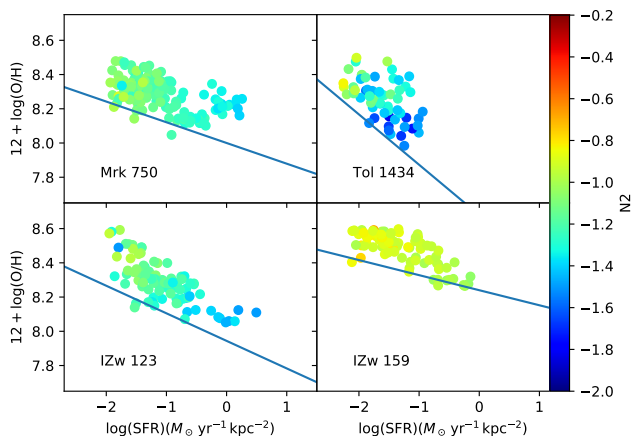


**Figure 7.** Same as Fig. 6, for four PMAS galaxies (see the labels). In this case the line  $[\text{OII}]\lambda 3727$  is included in the O/H determination. The anti-correlation between O/H and SFR that appears in Fig. 1 remains here. The solid lines show the linear fits to the anti-correlation in Fig. 1 ( $k$  and  $m$  in Table 2). The formal error bars provided by HIIC turn out to be around 0.05 dex.

Kauffmann et al. 2003; Pettini & Pagel 2004; Cid Fernandes et al. 2010). On the other hand, the location of data points on the BPT diagram is almost insensitive to reddening or mis-calibration, since the lines in each ratio are very close in wavelength and any multiplicative factor affecting the observed fluxes cancels out. We will argue that our galaxies occupy a region of the BPT plane consistent with a spread in metallicity, both comparing them with previous observations (this section) and with photoionization models (Sect. 4.3).

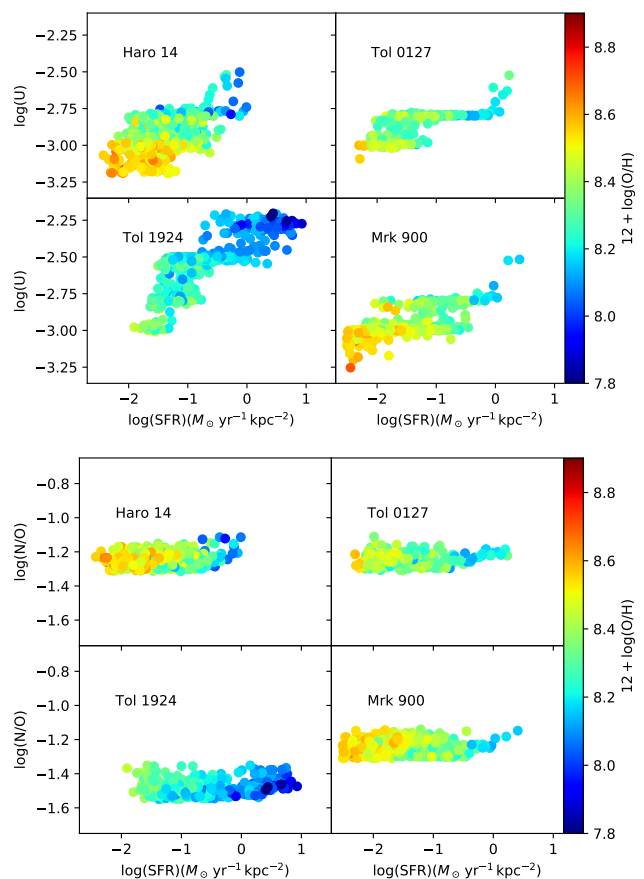


**Figure 8.** Top panels: Variation of the ionization parameter ( $U$ ) with SFR as inferred from HIIC for the galaxies in Fig. 6. There is a significant increase of  $U$  with increasing SFR. Bottom panels: Variation of N/O with SFR as inferred from HIIC. The ratio remains rather constant across the galaxy. The different spaxels are color-coded according to their  $12 + \log(\text{O}/\text{H})$  from HIIC, as indicated by the color bar. The range of ordinates corresponds to 1.1dex, which is the same range used in Figs. 6 and 7. The formal error bars provided by HIIC for  $\log(U)$  and  $\log(\text{N}/\text{O})$  turn out to be around 0.01 dex and 0.03 dex, respectively.

Sánchez et al. (2015) use a set of 5000 HII regions from the CALIFA survey (which includes galaxies of all masses and Hubble types; Sánchez et al. 2012), to explore the distribution of observed HII regions on the BPT diagram. Figure 9a shows the area of the BPT plane covered by these HII regions, and it is color-coded according to the mean metallicity of the regions that appear in that particular location of the plane. One can see a systematic variation which, among other things, indicates that the N2 index does indeed increase with increasing metallicity (as in Eq. [3]). The metallicities in Sánchez et al. were computed using the strong-line method by Pilyugin et al. (2012), which compares a number of emission lines with those observed in HII regions with metallicities determined through the direct method. Their values were also cross-checked with the O3N2 calibrator (e.g., Pettini & Pagel 2004). The two methods are independent of the N2 method used in our metallicity estimate.

Using the HII regions in CALIFA as reference, we find

that the individual spaxels of most of our galaxies cover a region of the BPT plane characterized by more than one metallicity. Examples are shown in Fig. 9b and 9d. These two panels display the metallicity mapping of the BPT by Sánchez et al., i.e., the same as Fig. 9a, but only in the region containing the spaxels of our galaxies. It is clear how the observed region corresponds to a range of metallicities. Figure 9c shows another galaxy (Mrk 32) where all the spaxels are concentrated in a small region of the BPT plane, and so they likely correspond to a single metallicity in the mapping. However, even in this second case, one cannot discard more than one metallicity, since many of the galaxy’s spaxels appear outside the BPT region covered by the CALIFA sample. From our set of 16 galaxies, 12 galaxies show a clear spread in metallicity (Haro 11, Haro 14, IZw 123, IZw 159, Mrk 206, Mrk 407, Mrk 409, Mrk 750, Mrk 900, Mrk 1418, Tol 127, and Tol 1937), whereas the remaining 4 objects do not (Mrk 32, Mrk 475, Tol 1434, and Tol 1924).

The above exercise was repeated using other empirical datasets to assign metallicities to each point of the BPT plane. Specifically, the galaxies employed for calibration by Pilyugin et al. (2012) allowed us to fit with a two-dimensional polynomial the scatter plot  $12 + \log(\text{O}/\text{H})$  versus N2 and O3. The fit assigns a metallicity to every pair N2 O3, which we then apply to the values observed in our galaxies to infer the expected  $12 + \log(\text{O}/\text{H})$ . The result of the exercise for Haro 14 is included in Fig. 10a, which shows how its N2 and O3 cover a region spanning a range of metallicities. The same conclusion is drawn when fitting the two-dimensional polynomial to the galaxies employed by Marino et al. (2013); see Fig. 10b. It is important to realize that the data used for calibration are based on the direct method where differences of physical parameters (electron density and temperature) and chemical composition (N/O) are self-consistently taken into account in the determination of metallicity.

In short, most of the galaxies analyzed in the paper have  $\log([\text{OIII}]\lambda 5007/\text{H}\beta)$  and  $\log([\text{NII}]\lambda 6583/\text{H}\alpha)$  values spreading over an area of the BPT diagram that corresponds to HII regions having a range in metallicities.

### 4.3 Comparison with numerical models

In the previous section we compare the observed line ratios with observed HII regions. Here we compare them with model HII regions. We wanted to check whether the line ratios observed in the galaxies are compatible with model HII regions having a realistic range of physical parameters but a single metallicity. The photoionization models by Kewley et al. (2013) were meant to explain the evolution of the galaxies on the BPT diagram when the redshift changes from 0 to 3. These models provide a fair reference to compare with since they scan a wide range of physical parameters which (a) reproduce the sequence followed by the local star-forming galaxies, and (b) include the extreme conditions that characterize high redshift objects. High redshifts galaxies are systematically displaced in the BPT with respect to local galaxies (e.g., Steidel et al. 2014; Kashino et al. 2017), and the need for the models to reach this region of the BPT plane guarantees sampling a large range of physical conditions. The position of the model galaxies on the BPT depends on the ionizing radiation field, the geometry of the emitting gas, the electron temperature and

density and, finally, on the metallicity. The radiation field itself depends on the IMF (Initial Mass Function) and on the age and metallicity of the stellar population. Kewley et al. use the Mappings photoionization code (e.g., Binette et al. 1985; Sutherland & Dopita 1993) to model O3 and N2 in the HII regions surrounding a large set of ionizing stellar clusters with different properties. They assume a Salpeter IMF with an upper mass limit of  $100 M_{\odot}$ , but this choice of IMF has negligible impact on the emission line ratios. The stellar model atmospheres include winds of massive stars and WR (Pauldrach et al. 2001; Hillier & Miller 1998), and Geneva evolutionary tracks (Meynet et al. 1994). The clusters have continuous star formation extending over 4 Myr. Dust in the gas-phase is included, metals are partly depleted into the dust grains, and  $\alpha$ -element abundances are assumed to scale with metallicity. The nebulae are radiation bounded and isobaric, with an electron density that varies from 10 to  $10^3 \text{ cm}^{-3}$ . The variation of the metallicity range with redshift is taken from cosmological numerical simulations of galaxy formation (Davé et al. 2011a,b). The photoionization models thus constructed have been thoroughly tested, and they reproduce the properties of the local star-forming galaxies (e.g., Kewley et al. 2001a; Levesque et al. 2010).

At each redshift  $z$ , the models by Kewley et al. predict a mean relation between O3 and N2 given by,

$$\text{O3} = 1.1 + 0.003 z + \frac{0.61}{\text{N2} + 0.08 - 0.1833 z}, \quad (16)$$

with the metallicity varying along the sequence as,

$$12 + \log(\text{O}/\text{H}) = 8.97 + 0.0663 z - (\text{O3} - \text{N2})(0.32 - 0.025 z). \quad (17)$$

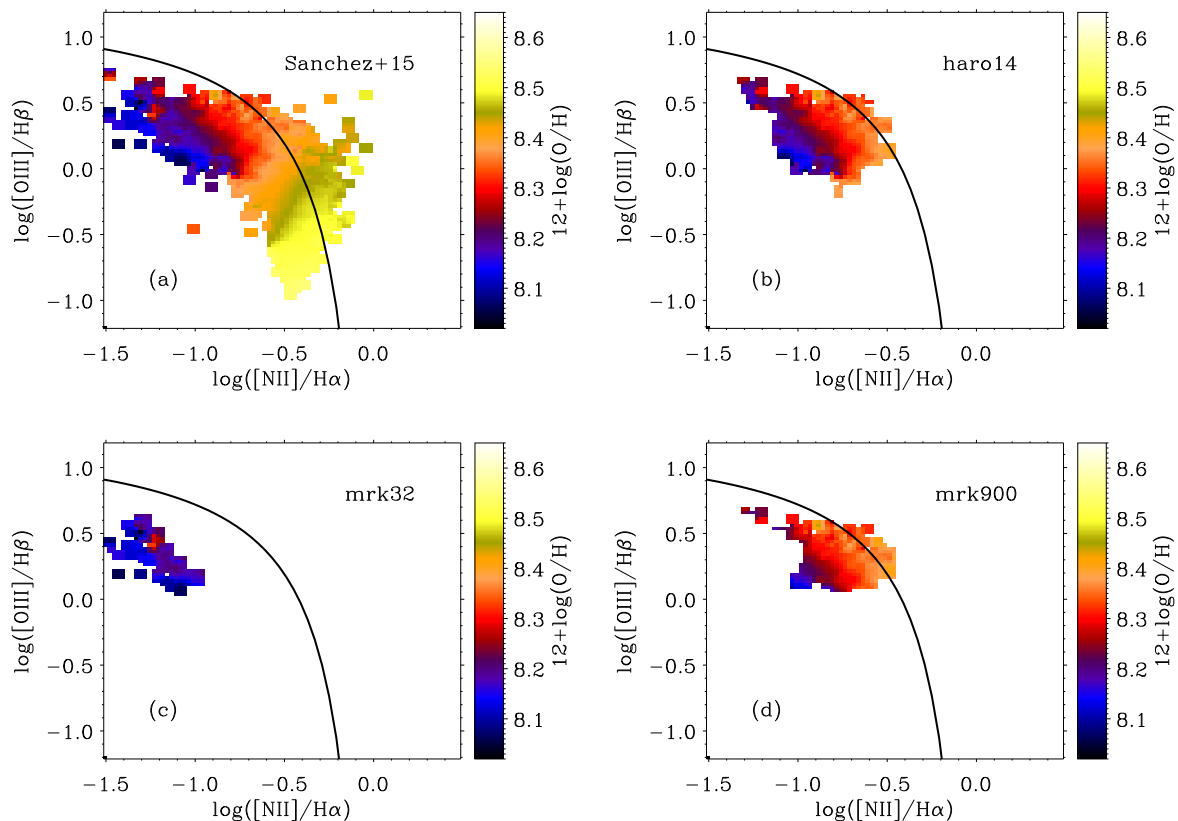
Thus, Eqs. (16) and (17) provide an implicit relation that gives  $12 + \log(\text{O}/\text{H})$  as a function of N2 and O3. Specifically, the relation gives the metallicity to be expected in a typical galaxy having specific values for N2 and O3. When the redshift varies from 0 to 3, the relation covers a substantial fraction of the BPT plane, shown as the colored region in Fig. 11.

Figure 11 shows the position of the spaxels of Haro 14 overlaid on the BPT diagram of these numerical photoionization models. The observed points do not follow ridges of constant metallicity. Instead, they appear in a region that corresponds to a range of metallicities of around 0.3 dex. The range of metallicity is similar to the range covered by Haro 14 on the observational BPT (Fig. 9, top right panel) as well as in our metallicity estimate (Figs. 1 and 6).

Haro 14 is just an example, but most galaxies have O3 and N2 spreading over an area of the BPT diagram that corresponds to HII regions with a range in metallicities. This need is not so clear in other cases like Mrk 32, which is the same conclusion reached when comparing the spread in O3 and N2 with observations (Fig. 9c).

## 5 DISCUSSION AND CONCLUSIONS

Based on the analysis of IFU data from 14 dwarf star-forming galaxies, we find a clear anti-correlation between the  $\text{H}\alpha$  flux in each spaxel and the value of N2. The anti-correlation is not due to noise in the spectra (Sect. 2). We attribute it to the existence of a relation between the local SFR (as traced by  $\text{H}\alpha$ ) and the metallicity of the gas used to



**Figure 9.** (a) Mean metallicity of the HII regions corresponding to each point in the BPT plane ( $\log([\text{OIII}]\lambda 5007/\text{H}\beta)$  versus  $\log([\text{NII}]\lambda 6583/\text{H}\alpha)$ ), as measured from  $\sim 5000$  HII regions from the CALIFA survey (Sánchez et al. 2015). The color bar gives the equivalence between color and metallicity, with each single color corresponding to a range of metallicity of  $\sim 0.05$  dex. (b) Same as (a) but showing only the area where the spaxels of Haro 14 appear. Note that the area shows several colors, and so it covers several metallicities. (c) Same as (b) for Mrk 32. In this case, all the spaxels of the galaxy are concentrated in an area with a single color, implying homogeneity in metallicity. However, many of the spaxels of this particular galaxy lie outside the range of  $\log([\text{OIII}]\lambda 5007/\text{H}\beta)$  and  $\log([\text{NII}]\lambda 6583/\text{H}\alpha)$  sampled by Sánchez et al. (2015). (d) Same as (b) for Mrk 900, which also shows metallicity variations. The solid line, shown for reference, is the same in all the panels. It corresponds to the divide worked out by Kauffmann et al. (2003) to separate star-forming galaxies from galaxies with AGN-like activity.

form stars (traced by N2). Each increase of the SFR by one order of magnitude is associated with a drop in metallicity of 0.15 dex (Eq. [5]).

The anti-correlation is set by local variations of N2 and H $\alpha$ , because it remains even if the large scale variation of these two quantities is subtracted out from the N2 and H $\alpha$  maps (Sect. 2.4). Thus, the anti-correlation is not produced by the radial drop in metallicity expected in spirals. Since the angular resolution of the individual maps is between 50 and 500 pc, the anti-correlation refers to integrated properties of entire HII regions. It does not arise from the internal (sub-)structure of the individual HII regions.

The relation between N2 and metallicity, and H $\alpha$  flux and SFR, are obtained from semi-empirical calibrations. The uncertainties inherent to the two calibrations may be correlated, thus faking a relation between metallicity and SFR. In order to discard this potential bias, a number of tests were carried out. We compute the metallicity using a technique which includes possible local variations in ionization parameter and N/O (Pérez-Montero 2014), and the anti-correlation between metallicity and SFR remains (Sect. 4.1).

We also compare the position of the galaxies in the so-called BPT diagram with the position of many observed HII regions having a large variety of metallicities (from Sánchez et al. 2015; Pilyugin et al. 2012; Marino et al. 2013). Our galaxies occupy an area corresponding to a range in metallicities of around 0.2 dex (Sect. 4.2). In addition, we compare the observations with photoionization models (Kewley et al. 2013), which suggest that a spread in metallicities is required to account for the location of the spaxels in the BPT plane.

We studied plausible physical scenarios that create a local anti-correlation between metallicity and surface SFR. Thus, the observed anti-correlation is consistent with local infall of metal-poor gas, provided that the external gas mass is comparable to the gas mass previously existing in each spaxel (Sect. 3.1). Within this scenario, reproducing the observations requires some random variability in the mass of external gas contributing to each spaxel. It also demands the metallicity of the external gas to be much smaller than the solar metallicity. In addition, we explore the effect of self-enrichment of the observed HII regions with metals produced in past star-formation episodes. In this case the anti-

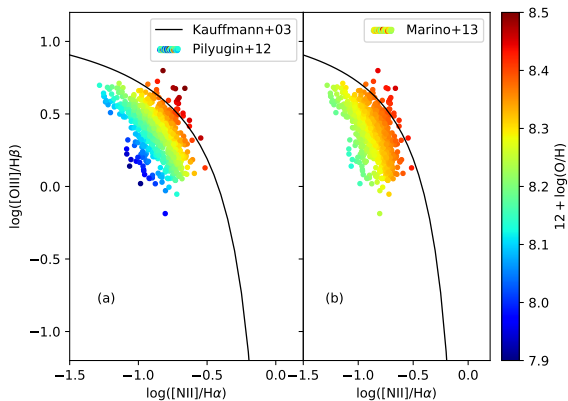


**Figure 10.** (a) BPT diagram of Haro 14 color-coded with the metallicity of galaxies from Pilyugin et al. (2012) having the same N2 and O3 as the individual spaxels in Haro 14. Note the need for a range of metallicities to explain the observed range of N2 and O3. (b) Same as (a) with the metallicity obtained from the galaxies used by Marino et al. (2013). The solid line corresponds to the divide below which star-forming galaxies appear (Kauffmann et al. 2003).

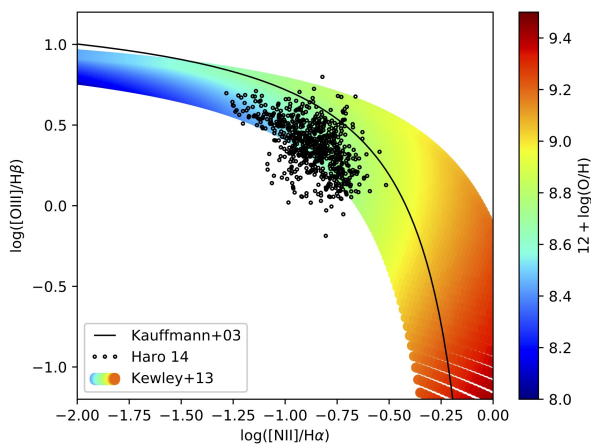


**Figure 11.** BPT diagram for Haro 14 (the open circles) overlaid on the numerical photoionization models by Kewley et al. (2013). The models are color-coded according to their gas-phase metallicity, as indicated by the color bar. The observed points occupy a region of the model BPT plane characterized by a range of metallicities of around 0.3 dex. The solid line separates star-forming galaxies from galaxies with AGN activity, according to Kauffmann et al. (2003). It is shown for reference and is the same as in Figs. 9 and 10.

correlation emerges because those regions very active in the past are now quiescent and metallic, with the opposite happening with the ones that were less effective (Sect. 3.2). If such self-enrichment is invoked as an explanation, then it comes with very intense outflows, having mass loading factors in excess of 10 (Eq. [15]). Even though we do not treat it explicitly in the main text, a combination of external metal-poor gas inflow plus self-enrichment should also render the observed anti-correlation.

Numerical simulations of galaxies formed in a cosmo-

logical context show how this type of local anti-correlation naturally results from the accretion of cosmological metal-poor gas that triggers star-formation bursts (Ceverino et al. 2016; Verbeke et al. 2014). Interpreting the observed relation in these terms is very appealing. However, it is not devoid of uncertainty since it involves either inefficient gas mixing in the galaxies showing the relation, or the recent accretion of metal-poor gas. The gas in the disk is expected to mix in a timescale of the order of the rotational period or smaller (e.g., de Avillez & Mac Low 2002; Yang & Krumholz 2012; Petit et al. 2015). Gas accretion, on the other hand, is theoretically predicted to fuel star formation in disk galaxies (e.g., Dekel et al. 2009; Silk & Mamon 2012), but the observational evidence of this process is still rather indirect (Sánchez Almeida et al. 2014a; Sánchez Almeida 2017). If the local anti-correlation between metallicity and SFR turns out to be universal, it would provide a strong support for the cosmological gas accretion predicted by these numerical models.

Curiously, the slope of the relation between metallicity and  $\log(\text{SFR})$  is similar to the slope for the cosmological evolution of these two quantities. The mean gas metallicity of the star-forming galaxies decreases by 0.15 dex when their redshift changes from 0 and 1 (Kewley & Kobulnicky 2007), while the SFR of the Universe increases by approximately one order of magnitude during this period (e.g., Madau & Dickinson 2014). The same slope is obtained from the variation with redshift of the metallicity and SFR in a group of relatively nearby low-mass irregular galaxies (redshift < 0.05; Pilyugin et al. 2013). The agreement may be coincidental, but we point it out because the change in the cosmic SFR probably follows the evolution of the cosmological gas accretion (e.g., Dekel et al. 2013; Sánchez Almeida et al. 2014a), and this cosmological process seems to produce an effect quantitatively similar to the local anti-correlation described in this work.

## ACKNOWLEDGEMENTS

We thank Sebastián Sánchez for providing some of the data used in Sect. 4.2, Enrique Pérez-Montero for help with the use of HIIC, and Matteo Miluzio for discussions and support during the early stages of the analysis. We also thank an anonymous referee whose comments help us improving the reliability of our argumentation. M.E.F. gratefully acknowledges the financial support of the *Fundação para a Ciência e Tecnologia* (FCT – Portugal), through the research grant SFRH/BPD/107801/2015. This work has been partly funded by the Spanish Ministry of Economy and Competitiveness, projects *Estalidos* AYA2013–47742–C04–02–P and AYA2016–79724–C4–2–P, as well as AYA2014–58861–C3–1–P.

## REFERENCES

- Amorín R., et al., 2014, *A&A*, 568, L8  
 Andrews B. H., Martini P., 2013, *ApJ*, 765, 140  
 Asplund M., Grevesse N., Sauval A. J., Scott P., 2009, *ARA&A*, 47, 481  
 Baldwin J. A., Phillips M. M., Terlevich R., 1981, *PASP*, 93, 5  
 Bell E. F., de Jong R. S., 2001, *ApJ*, 550, 212  
 Binette L., Dopita M. A., Tuohy I. R., 1985, *ApJ*, 297, 476



- Bothwell M. S., Maiolino R., Kennicutt R., Cresci G., Mannucci F., Marconi A., Ciccone C., 2013, *MNRAS*, **433**, 1425
- Bothwell M. S., Maiolino R., Ciccone C., Peng Y., Wagg J., 2016a, preprint, ([arXiv:1606.04102](https://arxiv.org/abs/1606.04102))
- Bothwell M. S., Maiolino R., Peng Y., Ciccone C., Griffith H., Wagg J., 2016b, *MNRAS*, **455**, 1156
- Bradley E., Tibshirani R. J., 1994, *An Introduction to the Bootstrap* (Monographs on Statistics and Applied Probability. Chapman and Hall/CRC, Boca Raton)
- Brisbin D., Harwit M., 2012, *ApJ*, **750**, 142
- Brown J. S., Martini P., Andrews B. H., 2016, *MNRAS*, **458**, 1529
- Burstein D., Heiles C., 1982, *AJ*, **87**, 1165
- Cairós L. M., Caon N., Vílchez J. M., González-Pérez J. N., Muñoz-Tuñón C., 2001, *ApJS*, **136**, 393
- Cairós L. M., Caon N., Zurita C., Kehrig C., Weibacher P., Roth M., 2009a, *A&A*, **507**, 1291
- Cairós L. M., Caon N., Papaderos P., Kehrig C., Weibacher P., Roth M. M., Zurita C., 2009b, *ApJ*, **707**, 1676
- Cairós L. M., Caon N., Zurita C., Kehrig C., Roth M., Weibacher P., 2010, *A&A*, **520**, A90+
- Cairós L. M., Caon N., Weibacher P. M., 2015, *A&A*, **577**, A21
- Cannon J. M., Skillman E. D., Kunth D., Leitherer C., Mas-Hesse M., Östlin G., Petrosian A., 2004, *ApJ*, **608**, 768
- Cardelli J. A., Clayton G. C., Mathis J. S., 1989, *ApJ*, **345**, 245
- Ceverino D., Sánchez Almeida J., Muñoz Tuñón C., Dekel A., Elmegreen B. G., Elmegreen D. M., Primack J., 2016, *MNRAS*, **457**, 2605
- Cid Fernandes R., Stasińska G., Schlickmann M. S., Mateus A., Vale Asari N., Schoenell W., Sodr e L., 2010, *MNRAS*, **403**, 1036
- Cresci G., Mannucci F., Maiolino R., Marconi A., Gnerucci A., Magrini L., 2010, *Nature*, **467**, 811
- Cullen F., Cirasuolo M., McLure R. J., Dunlop J. S., Bowler R. A. A., 2014, *MNRAS*, **440**, 2300
- Dav e R., Oppenheimer B. D., Finlator K., 2011a, *MNRAS*, **415**, 11
- Dav e R., Finlator K., Oppenheimer B. D., 2011b, *MNRAS*, **416**, 1354
- Dayal P., Ferrara A., Dunlop J. S., 2013, *MNRAS*, **430**, 2891
- De Rossi M. E., Theuns T., Font A. S., McCarthy I. G., 2015, *MNRAS*, **452**, 486
- Dekel A., et al., 2009, *Nature*, **457**, 451
- Dekel A., Zolotov A., Tweed D., Cacciato M., Ceverino D., Primack J. R., 2013, *MNRAS*, **435**, 999
- Ellison S. L., Patton D. R., Simard L., McConnachie A. W., 2008, *ApJ*, **672**, L107
- Ferland G. J., et al., 2013, *Rev. Mex. Astron. Astrofis.*, **49**, 137
- Filho M. E., S anchez Almeida J., Mu oz-Tu n n C., Nuza S. E., Kitaura F., He s S., 2015, *ApJ*, **802**, 82
- Forbes J. C., Krumholz M. R., Burkert A., Dekel A., 2014, *MNRAS*, **443**, 168
- Fraternali F., 2017, in Fox A., Dav e R., eds, *Astrophysics and Space Science Library* Vol. 430, *Astrophysics and Space Science Library*. p. 323 ([arXiv:1612.00477](https://arxiv.org/abs/1612.00477)), doi:10.1007/978-3-319-52512-9\_14
- Fuentes-Masip O., Mu oz-Tu n n C., Casta eda H. O., Tenorio-Tagle G., 2000, *AJ*, **120**, 752
- Gil de Paz A., Madore B. F., Pevunova O., 2003, *ApJS*, **147**, 29
- Hidalgo S. L., 2017, *A&A*, **606**, A115
- Hillier D. J., Miller D. L., 1998, *ApJ*, **496**, 407
- Hinojosa-Goi n R., Mu oz-Tu n n C., M endez-Abreu J., 2016, *A&A*, **592**, A122
- Hunt L. K., Hirashita H., 2009, *A&A*, **507**, 1327
- Izotov Y. I., Guseva N. G., Fricke K. J., Henkel C., 2014, *A&A*, **561**, A33
- Jimmy Tran K.-V., Saintonge A., Accurso G., Brough S., Oliva-Altamirano P., 2015, *ApJ*, **812**, 98
- Kacprzak G. G., et al., 2016, *ApJ*, **826**, L11
- Kashino D., Renzini A., Silverman J. D., Daddi E., 2016, *ApJ*, **823**, L24
- Kashino D., et al., 2017, *ApJ*, **835**, 88
- Kauffmann G., et al., 2003, *MNRAS*, **346**, 1055
- Kehrig C., et al., 2016, *MNRAS*, **459**, 2992
- Kennicutt Jr. R. C., 1998, *ARA&A*, **36**, 189
- Kennicutt R. C., Evans N. J., 2012, *ARA&A*, **50**, 531
- Kewley L., Koblunick H. A., 2007, *Astrophysics and Space Science Proceedings*, **3**, 435
- Kewley L. J., Dopita M. A., Leitherer C., Dav e R., Yuan T., Allen M., Groves B., Sutherland R., 2013, *ApJ*, **774**, 100
- Kunth D., Leitherer C., Mas-Hesse J. M.,  stlin G., Petrosian A., 2003, *ApJ*, **597**, 263
- Lagos P., Demarco R., Papaderos P., Telles E., Nigoche-Netro A., Humphrey A., Roche N., Gomes J. M., 2016, *MNRAS*, **456**, 1549
- Lara-L pez M. A., et al., 2010, *A&A*, **521**, L53
- Le F vre O., et al., 2003, in Iye M., Moorwood A. F. M., eds, *Proc. SPIE Vol. 4841, Instrument Design and Performance for Optical/Infrared Ground-based Telescopes*. pp 1670–1681, doi:10.1117/12.460959
- Lian J. H., Li J. R., Yan W., Kong X., 2015, *MNRAS*, **446**, 1449
- Lilly S. J., Carollo C. M., Pipino A., Renzini A., Peng Y., 2013, *ApJ*, **772**, 119
- L pez-S anchez  . R., 2010, *A&A*, **521**, A63
- Ly C., Malkan M. A., Nagao T., Kashikawa N., Shimasaku K., Hayashi M., 2014, *ApJ*, **780**, 122
- Ly C., Rigby J. R., Cooper M., Yan R., 2015, *ApJ*, **805**, 45
- MacHattie J. A., Irwin J. A., Madden S. C., Cormier D., R my-Ruyer A., 2014, *MNRAS*, **438**, L66
- Madau P., Dickinson M., 2014, *ARA&A*, **52**, A15
- Maier C., Lilly S. J., Ziegler B. L., Contini T., P rez Montero E., Peng Y., Balestra I., 2014, *ApJ*, **792**, 3
- Mannucci F., Cresci G., Maiolino R., Marconi A., Gnerucci A., 2010, *MNRAS*, **408**, 2115
- Marino R. A., et al., 2013, *A&A*, **559**, A114
- Markwardt C. B., 2009, in Bohlender D. A., Durand D., Dowler P., eds, *Astronomical Society of the Pacific Conference Series* Vol. 411, *Astronomical Data Analysis Software and Systems XVIII*. p. 251 ([arXiv:0902.2850](https://arxiv.org/abs/0902.2850))
- Meynet G., Maeder A., 2002, *A&A*, **390**, 561
- Meynet G., Maeder A., Schaller G., Schaerer D., Charbonnel C., 1994, *A&AS*, **103**, 97
- Moore D. S., McCabe G. P., Duckworth W. M., Sclove S. L., 2003, *The Practice of Business Statistics: Using Data for Decisions*. W. H. Freeman, New York
- Morales-Luis A. B., P rez-Montero E., S anchez Almeida J., Mu oz-Tu n n C., 2014, *ApJ*, **797**, 81
- Moran E. C., Shahinyan K., Sugarman H. R., V lez D. O., Eracleous M., 2014, *AJ*, **148**, 136
- Muratov A. L., et al., 2017, *MNRAS*, **468**, 4170
- Olmo-Garc a A., S anchez Almeida J., Mu oz-Tu n n C., Filho M. E., Elmegreen B. G., Elmegreen D. M., P rez-Montero E., M endez-Abreu J., 2017, *ApJ*, **834**, 181
- Osterbrock D. E., Ferland G. J., 2006, *Astrophysics of gaseous nebulae and active galactic nuclei. Astrophysics of gaseous nebulae and active galactic nuclei*, 2nd. ed. by D.E. Osterbrock and G.J. Ferland. Sausalito, CA: University Science Books, 2006
-  stlin G., Marquart T., Cumming R. J., Fathi K., Bergvall N., Adamo A., Amram P., Hayes M., 2015, *A&A*, **583**, A55
- Pagel B. E. J., Edmunds M. G., 1981, *ARA&A*, **19**, 77
- Paturel G., Petit C., Prugniel P., Theureau G., Rousseau J., Brouty M., Dubois P., Cambr sy L., 2003, *A&A*, **412**, 45
- Pauldrach A. W. A., Hoffmann T. L., Lennon M., 2001, *A&A*, **375**, 161
- Peeples M. S., Pogge R. W., Stanek K. Z., 2009, *ApJ*, **695**, 259
- P rez-Montero E., 2014, *MNRAS*, **441**, 2663

Pérez-Montero E., Contini T., 2009, *MNRAS*, **398**, 949  
Pérez-Montero E., Díaz A. I., 2005, *MNRAS*, **361**, 1063  
Petit A. C., Krumholz M. R., Goldbaum N. J., Forbes J. C., 2015, *MNRAS*, **449**, 2588  
Pettini M., Pagel B. E. J., 2004, *MNRAS*, **348**, L59  
Pilyugin L. S., Grebel E. K., Mattsson L., 2012, *MNRAS*, **424**, 2316  
Pilyugin L. S., Lara-López M. A., Grebel E. K., Kehrig C., Zinchenko I. A., López-Sánchez Á. R., Vílchez J. M., Mattsson L., 2013, *MNRAS*, **432**, 1217  
Pipino A., Lilly S. J., Carollo C. M., 2014, *MNRAS*, **441**, 1444  
Prestwich A. H., Jackson F., Kaaret P., Brorby M., Roberts T. P., Saar S. H., Yukita M., 2015, *ApJ*, **812**, 166  
Richards S. N., et al., 2014, *MNRAS*, **445**, 1104  
Romeo Velonà A. D., Sommer-Larsen J., Napolitano N. R., Antonuccio-Delogo V., Cielo S., Gavignaud I., Meza A., 2013, *ApJ*, **770**, 155  
Roth M. M., et al., 2005, *PASP*, **117**, 620  
Rubin K. H. R., 2017, in Fox A., Davé R., eds, *Astrophysics and Space Science Library* Vol. 430, *Astrophysics and Space Science Library*. p. 95 ([arXiv:1612.00805](https://arxiv.org/abs/1612.00805)), doi:10.1007/978-3-319-52512-9\_5  
Salim S., Lee J. C., Ly C., Brinchmann J., Davé R., Dickinson M., Salzer J. J., Charlot S., 2014, *ApJ*, **797**, 126  
Sánchez Almeida J., 2017, in Fox A., Davé R., eds, *Astrophysics and Space Science Library* Vol. 430, *Astrophysics and Space Science Library*. p. 67 ([arXiv:1612.00776](https://arxiv.org/abs/1612.00776)), doi:10.1007/978-3-319-52512-9\_4  
Sánchez Almeida J., Terlevich R., Terlevich E., Cid Fernandes R., Morales-Luis A. B., 2012, *ApJ*, **756**, 163  
Sánchez Almeida J., Muñoz-Tuñón C., Elmegreen D. M., Elmegreen B. G., Méndez-Abreu J., 2013, *ApJ*, **767**, 74  
Sánchez Almeida J., Elmegreen B. G., Muñoz-Tuñón C., Elmegreen D. M., 2014a, *A&ARv*, **22**, 71  
Sánchez Almeida J., Morales-Luis A. B., Muñoz-Tuñón C., Elmegreen D. M., Elmegreen B. G., Méndez-Abreu J., 2014b, *ApJ*, **783**, 45  
Sánchez Almeida J., et al., 2015, *ApJ*, **810**, L15  
Sánchez Almeida J., Pérez-Montero E., Morales-Luis A. B., Muñoz-Tuñón C., García-Benito R., Nuza S. E., Kitaura F. S., 2016, *ApJ*, **819**, 110  
Sánchez S. F., et al., 2012, *A&A*, **538**, A8  
Sánchez S. F., et al., 2013, *A&A*, **554**, A58  
Sánchez S. F., et al., 2014, *A&A*, **563**, A49  
Sánchez S. F., et al., 2015, *A&A*, **574**, A47  
Sanders R. L., et al., 2015, *ApJ*, **799**, 138  
Schlegel D. J., Finkbeiner D. P., Davis M., 1998, *ApJ*, **500**, 525  
Schmitt H. R., Calzetti D., Armus L., Giavalisco M., Heckman T. M., Kennicutt Jr. R. C., Leitherer C., Meurer G. R., 2006, *ApJ*, **643**, 173  
Silk J., Mamon G. A., 2012, *Research in Astronomy and Astrophysics*, **12**, 917  
Simpson R. J., et al., 2012, *MNRAS*, **424**, 2442  
Steidel C. C., et al., 2014, *ApJ*, **795**, 165  
Sutherland R. S., Dopita M. A., 1993, *ApJS*, **88**, 253  
Tinsley B. M., 1980, *Fundamentals Cosmic Phys.*, **5**, 287  
Troncoso P., et al., 2014, *A&A*, **563**, A58  
Veilleux S., Cecil G., Bland-Hawthorn J., 2005, *ARA&A*, **43**, 769  
Verbeke R., De Rijcke S., Koleva M., Cloet-Osselaer A., Vandebroucke B., Schroyen J., 2014, *MNRAS*, **442**, 1830  
Villaverde M., Cerviño M., Luridiana V., 2010, *A&A*, **517**, A93  
Vogt F. P. A., Dopita M. A., Borthakur S., Verdes-Montenegro L., Heckman T. M., Yun M. S., Chambers K. C., 2015, *MNRAS*, **450**, 2593  
Wisnioski E., Glazebrook K., Blake C., Poole G. B., Green A. W., Wyder T., Martin C., 2012, *MNRAS*, **422**, 3339  
Wu Y.-Z., Zhang S.-N., Zhao Y.-H., Zhang W., 2016, *MNRAS*, **457**, 2929

Yabe K., et al., 2012, *PASJ*, **64**, 60

Yang C.-C., Krumholz M., 2012, *ApJ*, **758**, 48

Yates R. M., Kauffmann G., Guo Q., 2012, *MNRAS*, **422**, 215

de Avillez M. A., Mac Low M.-M., 2002, *ApJ*, **581**, 1047

de los Reyes M. A., et al., 2015, *AJ*, **149**, 79

## APPENDIX A: $M_{G2}/M_G$ WHEN $M_{G2}$ VARIES FROM SPAXEL TO SPAXEL

In Sect. 3.1, we explore the correlation between  $Z$  and SFR resulting from the mixing of pre-existing gas with external metal-poor gas. In the extreme case where the pre-existing gas-mass,  $M_{g2}$ , is the same for all the spaxels of the galaxy, then one expects a scaling of  $Z$  as  $1/M_g$ , with  $M_g$  the total gas mass in the spaxel. However, when  $M_{g2}$  varies, the correlation of  $Z$  with  $M_g$  weakens since  $M_g$  varies not only with the mass of external metal-poor gas,  $M_{g1}$ , but also with  $M_{g2}$  ( $M_g = M_{g1} + M_{g2}$ ). This can be formulated in mathematical terms considering that  $Z$  scales as  $M_{g2}/M_g$  (Eqs. [8] and [7]), so that when  $M_{g2}$  varies, then  $M_{g2}/M_g$  varies as

$$M_{g2}/M_g \propto M_g^{-\delta}, \quad (\text{A1})$$

with  $\delta < 1$ . The extreme case of constant  $M_{g2}$  corresponds to  $\delta = 1$ , whereas the case where the contribution of the external mass is negligible (i.e.,  $M_{g1} \ll M_{g2}$ ) gives  $\delta \sim 0$ . In order to explore the validity of the approximation in Eq. (A1), we carried out a series of Monte Carlo simulations that assume  $M_{g1}$  and  $M_{g2}$  to be two random variables, and then we study how  $M_{g2}/M_g$  depends on  $M_g$ . Independently of the distribution function assumed for the variables, one finds a relation between the mean  $M_{g2}/M_g$  for a given  $M_g$  that can be parameterized as in Eq. (A1). Figure A1 shows one example. In this particular case  $M_{g1}$  and  $M_{g2}$  are drawn from the positive wing of a Gaussian probability distribution function (PDF), with the mean and the dispersion of  $M_{g1}$  1.5 times larger than the mean and dispersion of  $M_{g2}$ . The resulting bidimensional PDF is displayed as an image in Fig. A1. The mean  $M_{g2}/M_g$  for each  $M_g$  is shown as a solid green line, with the 1-sigma dispersion around this mean represented as dotted green lines. A fit to this relation is shown as the red dashed line, and it corresponds to  $\delta \approx 0.3$ . The curve representing the extreme case where  $\delta = 1$  (i.e.,  $M_{g2}/M_g \propto 1/M_g$ ) is shown as a solid blue line.

This paper has been typeset from a  $\text{\TeX}/\text{\LaTeX}$  file prepared by the author.

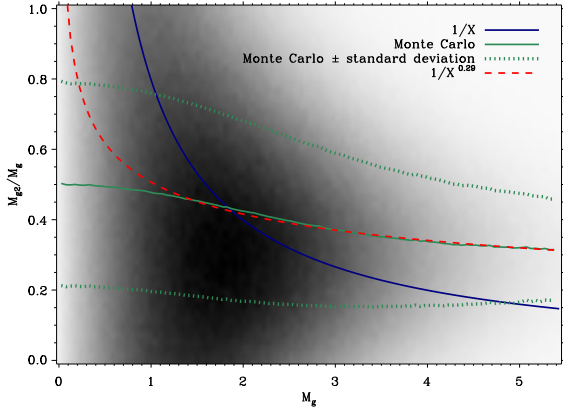


**Figure A1.**  $M_{g2}/M_g$  versus  $M_g$  in a Monte Carlo simulation where both  $M_{g1}$  and  $M_{g2}$  are random variables extracted from the positive wing of a Gaussian PDF, where the mean and the dispersion of  $M_{g1}$  is 1.5 times larger than the mean and dispersion of  $M_{g2}$ . The mean  $M_{g2}/M_g$  for each  $M_g$  is shown as a solid green line, with the 1-sigma dispersion around this mean represented as dotted green lines. The red dashed line shows a fit to this relation, which renders  $\delta \approx 0.3$ . The curve corresponding to  $\delta = 1$  (i.e.,  $M_{g2}/M_g \propto 1/M_g$ ) is shown for reference as a solid blue line. Masses are given in arbitrary units.